

Performance of Two-Moment Stratiform Microphysics With Prognostic Precipitation in GFDL's CM4.0

Huan Guo¹, Yi Ming¹, Songmiao Fan¹, Andrew T. Wittenberg¹, Rong Zhang¹, Ming Zhao¹, and Linjong Zhou²

¹NOAA/OAR/Geophysical Fluid Dynamics Laboratory, Princeton, NJ, USA, ²Cooperative Institute for Modeling the Earth System, Program in Oceanic and Atmospheric Sciences, Princeton University, Princeton, NJ, USA

Key Points:

- The performance of two-moment microphysics with prognostic precipitation and an ice nucleation scheme in CM4.0: CM4-MG2, is documented
- The overall performance of CM4-MG2 is comparable to or better than CM4.0, based on a set of Model Intercomparison Project Phase 6 Diagnosis, Evaluation, and Characterization of Klima and historical simulations
- Notable improvements include enhanced coastal stratocumulus and stronger Madden-Julian Oscillation. CM4-MG2 has a lower climate sensitivity than CM4.0

Correspondence to:

H. Guo,
huan.guo@noaa.gov

Citation:

Guo, H., Ming, Y., Fan, S., Wittenberg, A. T., Zhang, R., Zhao, M., & Zhou, L. (2022). Performance of two-moment stratiform microphysics with prognostic precipitation in GFDL's CM4.0. *Journal of Advances in Modeling Earth Systems*, 14, e2022MS003111. <https://doi.org/10.1029/2022MS003111>

Received 30 MAR 2022

Accepted 11 DEC 2022

© 2022 The Authors. This article has been contributed to by U.S. Government employees and their work is in the public domain in the USA.

This is an open access article under the terms of the [Creative Commons Attribution-NonCommercial-NoDerivs License](https://creativecommons.org/licenses/by/4.0/), which permits use and distribution in any medium, provided the original work is properly cited, the use is non-commercial and no modifications or adaptations are made.

Abstract We describe the model performance of a new global coupled climate model configuration, CM4-MG2. Beginning with the Geophysical Fluid Dynamics Laboratory's fourth-generation physical climate model (CM4.0), we incorporate a two-moment Morrison-Gettelman bulk stratiform microphysics scheme with prognostic precipitation (MG2), and a mineral dust and temperature-dependent cloud ice nucleation scheme. We then conduct and analyze a set of fully coupled atmosphere-ocean-land-sea ice simulations, following Coupled Model Intercomparison Project Phase 6 protocols. CM4-MG2 generally captures CM4.0's baseline simulation characteristics, but with several improvements, including better marine stratocumulus clouds off the west coasts of Africa and North and South America, a reduced bias toward “double” Intertropical Convergence Zones south of the equator, and a stronger Madden-Julian Oscillation (MJO). Some degraded features are also identified, including excessive Arctic sea ice extent and a stronger-than-observed El Niño-Southern Oscillation. Compared to CM4.0, the climate sensitivity is reduced by about 10% in CM4-MG2.

Plain Language Summary A sophisticated cloud microphysical scheme, along with a mineral dust and temperature-dependent ice nucleation scheme, have been implemented in a new configuration of the Geophysical Fluid Dynamics Laboratory's most recent climate model (CM4.0). This microphysical scheme predicts both mass and number concentrations of cloud drops, ice crystals, rain, and snow, and treats aerosol-cloud interactions more consistently. The ice nucleation on mineral dust aerosol in large-scale clouds is represented more realistically. Centennial-scale global coupled atmosphere-ocean-land-sea ice simulations from this new configuration compare favorably with observations—with improved subtropical stratocumulus clouds and better tropical intraseasonal variability (i.e., the 30- to 90-day Madden-Julian Oscillation). The new configuration also reduces the magnitude of future global warming in response to anthropogenic emissions.

1. Introduction

The pioneering development of coupled atmospheric and oceanic models was carried out in the late 1960s and 1970s (Manabe & Bryan, 1969; Manabe et al., 1975), followed by considerable advances in the 1980s and 1990s (Manabe & Stouffer, 1988). With rapidly growing computational power in recent decades, coupled models have experienced significant improvements due to higher resolution, more components, advanced complexity, evolution away from empirical relationships/corrections, and large ensemble simulations (IPCC, 2021). Nowadays they are widely adopted in climate studies. During the last 20 years, the model development at the Geophysical Fluid Dynamics Laboratory (GFDL) has built upon the Flexible Modeling System (Balaji, 2012), a common software infrastructure where large teams collaborate while groups/individuals specialize in a particular model component. This collaborative distributed development effort produced the most recent generations of GFDL's coupled models, for example, CM2.1, CM3, CM4.0 (Delworth et al., 2006; Donner et al., 2011; Held et al., 2019). CM4.0 is GFDL's fourth-generation general circulation model (GCM), participating in the Coupled Model Intercomparison Project Phase 6 (Eyring et al., 2016). With successive upgrades in its model components (Adcroft et al., 2019; Milly et al., 2014; Shevliakova et al., 2009; M. Zhao et al., 2018a; M. Zhao et al., 2018b), CM4.0 presents high-fidelity simulations of top-of-atmosphere (TOA) radiative fluxes, mean atmospheric state, Intertropical Convergence Zone (ITCZ), El Niño-Southern Oscillation (ENSO), ocean boundary currents, among others (Held et al., 2019).

However, there have been limited upgrades in the bulk cloud microphysics of the atmospheric component since the second-generation model of CM2.1 (Delworth et al., 2006). Bulk microphysical schemes only treat one or

more moments of cloud particles, or bulk properties of clouds (e.g., cloud mass). They were pioneered by E. Kessler et al. (1963). Since the 1970s, major developments in bulk schemes in GCMs have included ice microphysics, prognosing one or more species of cloud water, prognostic precipitation, and two-moment (mass and number) schemes with linkages to aerosols. In the late 1990s and 2000s, a partial two-moment scheme, that is, mass concentration plus number concentration of cloud water but not ice species, was widely used in GCMs with the goal of improving aerosol-cloud interactions (Ghan et al., 1997; Ming et al., 2006; Storelvmo et al., 2006). The cloud microphysics in CM4.0 is partially two-moment with diagnostic precipitation and is referred to as the Rotstajn-Klein (RK) scheme (Donner et al., 2011; GFDL Global Atmosphere Model Development Team, 2004; Golaz et al., 2011; Jakob & Klein, 2000; L. D. Rotstajn, 1997; L. Rotstajn et al., 2000).

The RK scheme prognoses the mass mixing ratios of cloud water and ice as well as cloud droplet number concentration, while the mass mixing ratios of rain and snow are diagnosed. The diagnostic precipitation treatment is efficient computationally, but there are a few issues. First, it distorts the relative importance of autoconversion and accretion for rain formation. Rain is diagnosed and removed in a single model time step, artificially suppressing accretion that depends on existing rain water and shifting the rain formation toward autoconversion. This does not conform to the observational constraint on the process level (Gettelman et al., 2013, 2015b). Second, the bias toward autoconversion likely amplifies aerosol indirect effects, because the autoconversion strongly depends on droplet size distribution and/or number concentration. The overestimate of autoconversion is one reason why the response of liquid water path (LWP) to aerosols is too strong (positive) in many GCMs (Quaas et al., 2009; M. Wang et al., 2012). Recent satellite observations and global cloud-resolving model simulations have also suggested that aerosol indirect effects might have been overestimated because the response of LWP to aerosols could be either positive or negative or neutral (Sato et al., 2018; Toll et al., 2019). Third, the neglect of precipitation advection is problematic in high-resolution atmospheric models. For example, given a 10 m s^{-1} horizontal wind speed and a 1 m s^{-1} fall velocity, falling 2 km means that precipitation has been advected to another grid box for horizontal grid spacing finer than 20 km. Hence the advection of precipitation is important as model resolution becomes more and more refined.

Furthermore, the RK scheme does not treat ice crystal number concentration (N_i) explicitly. Instead, it approximates N_i based on Meyers et al. (1992) in parameterizing Wegener-Bergeron-Findeisen (WBF) process. The concerns about the Meyers scheme are mainly two-fold in GFDL's Atmosphere Model version 4.0 (AM4.0). First, the Meyers ice nucleation scheme depends on temperature or ice supersaturation, not on aerosols. Hence the aerosol effects on ice clouds are missing. Second, the annual mean N_i estimated with the Meyers scheme is likely biased high, leading to a fast WBF conversion of supercooled liquid to ice. As a result, the supercooled liquid cloud fraction in the mixed-phase cloud regime is biased low when compared to satellite observations (Fan et al., 2019). As pinpointed by Tan et al. (2016), the supercooled fraction is closely linked to cloud-phase feedback via glaciation rate, and thus impacts the estimate of climate sensitivity and the fidelity of current and future climate simulations.

In order to address these issues and represent the aerosol indirect effects more realistically, Guo et al. (2021) implemented the cloud microphysics following Gettelman et al. (2015a) (MG2 hereafter), and ice nucleation parameterization following Fan et al. (2019) into AM4.0. This configuration is termed AM4-MG2. MG2 is a bulk scheme by assuming that cloud particles follow a gamma distribution. It explicitly predicts the mass mixing ratios and number concentrations (two moments) of cloud water, ice, rain, and snow. Therefore, it is expected to treat the aerosol-cloud interactions more consistently. Moreover, the temperature- and dust-dependent ice nucleation parameterization from Fan et al. (2019) is obtained by fitting air parcel model results, which agree well with laboratory experiments and in situ aircraft measurements. The air parcel model considers deposition nucleation, condensation nucleation, and immersion freezing on mineral dust particles. It turns out that AM4-MG2 simulations show weaker (less negative) aerosol radiative effects, more realistic supercooled liquid fraction, and improved stratocumulus clouds.

As a follow-up, we have applied the AM4-MG2 configuration under the coupled model framework of CM4.0, referred to as CM4-MG2. This paper aims to document the model performance and simulation characteristics of CM4-MG2. We give brief descriptions of the model components in Section 2. Section 3 discusses the CM4-MG2 fully coupled atmosphere-ocean-land-sea ice global simulation results, including pre-industrial control simulation, model mean climate of recent decades (1980–2014), climate variability, the twentieth century warming, and

climate sensitivity and cloud feedback, as well as comparison to the base model CM4.0. Finally, a summary of results is given in Section 4.

2. Model Description of CM4-MG2

2.1. Atmospheric Component

The atmospheric component of CM4-MG2 is based on AM4.0 (M. Zhao et al., 2018b; M. Zhao et al., 2018a). It uses the hydrostatic version of the GFDL Finite-Volume Cubed-Sphere (FV3) Dynamical Core (FV3) (L. Harris et al., 2020; Lin, 2004; Putman & Lin, 2007). The longwave radiation code adopts the simplified exchange approximation with updated spectral information and inclusion of CO₂ 10 μm band (Fels & Schwarzkopf, 1975; Schwarzkopf & Fels, 1991). The shortwave code employs the 18-band formulation with updated H₂O, CO₂ and O₂ formulations and inclusion of the shortwave water vapor continuum and CH₄ and N₂O absorption (Freidenreich & Ramaswamy, 2005; Paynter & Ramaswamy, 2012, 2014). With these updates, the shortwave absorption error is reduced down to 1% within the line-by-line benchmark calculation (M. Zhao et al., 2018a). Orographic gravity wave drag parameterization allows for arbitrary topography and considers nonlinear effects (Garner, 2005, 2018). Nonorographic gravity wave drag is parameterized following Alexander and Dunkerton (1999). The turbulent diffusivity in the planetary boundary layer is parameterized following Lock et al. (2000).

The bulk aerosol scheme, including 17 transported aerosol tracers, is similar to that in GFDL's Atmosphere Model version 3 (AM3) (Donner et al., 2011), but with a “light” chemistry that turns off photochemistry and stratospheric chemistry (Salzmann et al., 2010; M. Zhao et al., 2018a). Aerosols are simulated from emissions using prescribed ozone and other oxidants (e.g., OH), and are linked to the cloud microphysics through the parameterization of droplet activation. The droplet activation depends on aerosol mass, chemical composition, and vertical velocity, following the parameterization detailed in Ming et al. (2006, 2007).

The cloud macrophysics solves prognostic equations for cloud fraction and large-scale condensate: liquid and ice (Tiedtke, 1993), which are inputs for the MG2 cloud microphysics. The MG2 microphysics then converts the condensate to precipitation. The precipitation efficiency of MG2 impacts the humidity of the atmosphere, and thereby cloud macrophysics. Both shallow convection and deep convection are uniformly treated by a “double-plume” scheme, with strong/weak lateral mixing rate for shallow/deep plume (M. Zhao et al., 2016; M. Zhao et al., 2018b). The mixing affects convective precipitation efficiency, which impacts the amount of condensate for convective precipitation. The non-precipitated condensate is detrained and acts as a source term for large-scale cloud liquid or ice. The detrainment of liquid, ice, and drop number depends on the detrained mass flux and the specific humidity/number concentration difference between convective updrafts and large-scale clouds. The convective detrainment is a key aspect of the connection between convection and the large-scale MG2 microphysics.

Important changes in the atmospheric component from CM4.0 to CM4-MG2 include:

1. The replacement of the RK cloud microphysics with the MG2 microphysics.
2. The incorporation of the mineral dust and temperature-dependent ice nucleation parameterization (Fan et al., 2019).
3. The inclusion of convective detrainment of ice number. The detrained ice number concentration depends on the detrained ice mass mixing ratio and temperature (Kristjansson et al., 2000; Salzmann et al., 2010).
4. The inclusion of the sedimentation of both number and mass of cloud water, ice, rain, and snow (Morrison & Gettelman, 2008). A time-implicit numerical scheme is applied for the hydrometeor sedimentation. The implicit scheme is more efficient computationally and stable numerically, but more diffusive (see the detailed comparison of implicit and explicit sedimentation treatments in Appendix A in Guo et al. (2021)).
5. The consideration of rain and snow radiative effects. The shortwave radiative properties of rain are based on the Mie theory (Savijarvi, 1997), while the shortwave radiative properties of snow are parameterized following Fu et al. (1995). The longwave properties of rain and snow are derived assuming that rain and snow are spherical particles.

Additionally, we adjusted a few parameters related to cloud microphysics and macrophysics, aerosol activation, and convection parameterizations (see Appendix A for model tunings in CM4-MG2). These parameter adjustments are regarded as within observational or conceptual uncertainties, or agree with previous studies. For

Table 1
Summary of CM4-MG2 Fully Coupled Atmosphere-Ocean-Land-Sea Ice Simulations

Experiment	Description	Period (years)	Ensemble size	Initialization
piControl	Pre-industrial control	500	1	piControl spinup
1pctCO2	CO ₂ prescribed to increase at 1%/yr	150	1	piControl (101)
abrupt-4xCO2	CO ₂ abruptly quadrupled and then held constant	150	1	piControl (101)
Historical	Coupled historical	1850–2014	3	piControl (101, 140, 182)

example, an important source/sink for ice is sedimentation. A scaling factor for ice fall velocity is set to 1.5 in AM3, to 0.9 in AM4.0/CM4.0, and to 0.91 in CM4-MG2 (Donner et al., 2011; M. Zhao et al., 2018b). The MG2 microphysics does not consider the correlation between cloud water and rain water, and therefore underestimates accretion process rate (Lebsock et al., 2013). In CM4-MG2, the accretion rate is boosted by a factor of 1.3, which enhances the ratio of accretion over autoconversion and reduces the magnitude of aerosol indirect effect. For the autoconversion parameterization, we employ the Seifert and Beheng (2001) scheme, which enhances subtropical stratocumulus clouds off the west coasts. Subgrid vertical velocity plays a crucial role on cloud droplet number concentration and aerosol indirect effect (Golaz et al., 2011). The minimum standard deviation of sub-grid vertical velocity is reduced to 0.3 m s⁻¹ as used in Storelvmo et al. (2006), Salzmann et al. (2010). The Tiedtke cloud macrophysics includes a sink term or “erosion term” to account for subgrid-scale mixing that dissipates clouds in sub-saturated grid cells. The erosion constant under convective conditions is tuned to $4.7 \times 10^{-6} \text{ s}^{-1}$ as used in AM2 (GFDL Global Atmosphere Model Development Team, 2004). The lateral mixing rate in the deep convective plume is an important factor affecting the spatial distribution of precipitation. Increasing the lateral mixing rate to 1.1 km⁻¹ leads to less penetrative plumes and weaker convective precipitation. The conversion efficiency of ice to snow in convective plumes is changed to $13 \times 10^{-5} \text{ Pa}^{-1}$, in order to reduce outgoing longwave radiation (OLR) biases in tropics. Details on the atmospheric component of CM4-MG2 are available in the AM4-MG2 documentation paper by Guo et al. (2021).

2.2. Land, Ocean, and Sea Ice Components

The remaining components in CM4-MG2 are identical to those in CM4.0 (Held et al., 2019). The land component is referred to as LM4.0.1, which is similar to LM4.0 as documented in M. Zhao et al. (2018a); M. Zhao et al. (2018b) but with dynamic vegetation, enhanced snow-covered glacial albedo, and tiling structure interacting with atmosphere. The ocean component: OM4p25, is described in Adcroft et al. (2019). It uses a hybrid depth-isopycnal coordinate (Adcroft & Hallberg, 2006; Bleck, 2002), and about 25 km horizontal resolution without mesoscale eddy parameterization. The sea ice component adopts the Sea Ice Simulator version 2 (SIS2) (Adcroft et al., 2019), which is based upon the earlier sea ice model version employed in CM2 (Delworth et al., 2006). But the code is completely rewritten and contains many ice physics changes. SIS2 shares the same horizontal grid layouts (i.e., the Arakawa C-grid) as OM4p25, but with four sea ice layers and one snow layer vertically. There are 5 sea ice thickness categories bounded at 0.1, 0.3, 0.7, and 1.1 m. The thinnest category extends down to zero and the thickest is unbounded. These 5 categories are concentrated in the low sea ice thickness categories, because of the lack of a subgrid ice ridging scheme (Adcroft et al., 2019).

3. Model Simulations and Results

With CM4-MG2, we have conducted a suite of fully coupled atmosphere-ocean-land-sea ice CMIP6 Diagnosis, Evaluation, and Characterization of Klima (DECK) and historical simulations (Eyring et al., 2016), including 500-year pre-industrial control (piControl), 150-year CO₂ concentration increasing 1% per year (1pctCO2), 150-year abruptly quadrupled CO₂ (abrupt-4xCO2), and three historical ensemble (1850–2014) simulations (Table 1). The piControl experiment was initialized from the piControl spinup run at year 151, and was driven by the fixed forcing levels at 1850. The piControl spinup follows the same procedure as in CM4.0 where atmosphere and land states were from a 700-year piControl simulation with prototype configurations, and ocean and sea ice were based on the World Ocean Atlas January climatology (Antonov et al., 2006; Held et al., 2019; Locarnini et al., 2006). Given the computational costs of fully coupled simulations, we have only one ensemble member for the 1pctCO2 experiment, one member for the abrupt-4xCO2 experiment, and three members for the historical

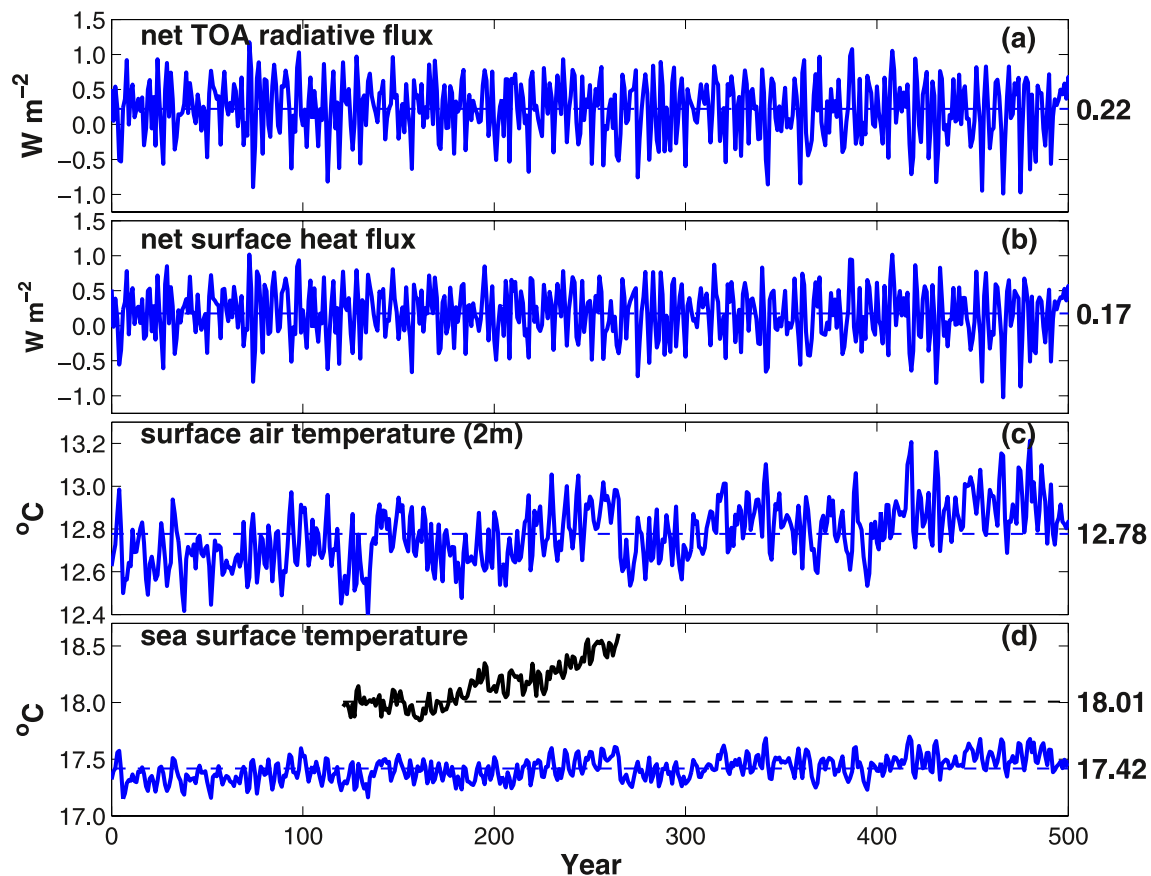


Figure 1. Time series of annual (a) global mean net radiative flux at top-of-atmosphere (positive down), (b) global mean net heat flux at surface, (c) global mean surface air temperature, and (d) global mean sea surface temperature. Blue solid lines represent the 500-year time series of the CM4-MG2 piControl experiment. Blue dashed is the 500-year average of the CM4-MG2 piControl. Black solid is the time evolution (1870–2014) of the Hadley Center Sea Ice and Sea Surface Temperature data set (HadISST) (Rayner et al., 2003). Black dashed line is the time average of HadISST over 1880–1990.

experiment. The 1pctCO₂ and abrupt-4xCO₂ experiments were branched off the piControl at year 101. The three historical realizations share the same ocean, sea ice, and land initial conditions spun off the piControl at year 101; but differ in the atmosphere initial condition which came from the piControl restart spaced by about 40 years (i.e., piControl Years 101, 140, and 182, respectively).

All coupled simulations discussed in this study were run at nominal 1.0° horizontal resolution (or about 100 km) for atmosphere and land, and 0.25° horizontal resolution for ocean and sea ice. The atmospheric component uses 33 levels with a relatively “low top” of about 1 hPa in the vertical, while the ocean component has 75 vertical layers with about 2 m vertical spacing near the ocean surface and 250 m below 5,000 m. The atmospheric physics time step is 30 min with two substeps (i.e., 15 min) for the microphysical processes. Ocean baroclinic and barotropic time steps are 15 min and about 19 s, respectively. The coupling frequency for all components is every 30 min.

3.1. Pre-Industrial Control Experiment

In this section we will discuss the global-scale evolution of the CM4-MG2 piControl simulation. Figure 1a provides the net downward radiative flux at TOA. The TOA radiative flux generally fluctuates between -1.0 and $+1.0$ W m^{-2} with little model drift. Its 500-year average is about 0.22 W m^{-2} . We also calculate the net heat flux out of the atmosphere at the surface, which is stable with an average of about 0.17 W m^{-2} over the 500-year period. The non-zero difference between the TOA and surface fluxes suggests an artificial energy sink of 0.05 W m^{-2} in the CM4-MG2 model atmosphere (vs. 0.08 W m^{-2} in CM4.0). This sink stems from the inconsistent definitions of energy conservation between model dynamics and physics. For example, the atmospheric dynamic core considers

the heat capacity for the total air (including condensed water) and the temperature dependence of latent heat, but atmospheric physics does not (Lin, 2004; Putman & Lin, 2007; Yano & Maarten, 2017; Zhou et al., 2019). An energy fix term for this inconsistency has been introduced in the Atmospheric Model Intercomparison Project (AMIP) mode, but gives rise to an energy sink (or imbalance) in the fully coupled mode (Held et al., 2019). However, the energy imbalance here is small relative to the radiative forcing caused by anthropogenic emissions, so we do not expect it would impose significant impacts on the model climate (Golaz et al., 2019).

Figures 1c and 1d present the time evolution of the global mean surface air temperature at 2 m (T_{air}) and sea surface temperature (SST) from the OM4p25 outputs. Both T_{air} and SST show slightly warming trends ($+0.018^{\circ}\text{C}/\text{century}$ for T_{air} and $+0.015^{\circ}\text{C}/\text{century}$ for SST). This is partly associated with the Southern Ocean that has not reached the equilibrium or steady state in the CM4-MG2 piControl, similar to what is reported in Held et al. (2019). Compared to the HadISST over 1880–1900 ($18.00 \pm 0.06^{\circ}\text{C}$), the CM4-MG2's SST ($17.42 \pm 0.10^{\circ}\text{C}$) is biased low by about 0.58°C (vs. 0.62°C low bias in CM4.0). In the AMIP simulations where the SST is prescribed (M. Zhao et al., 2018a), T_{air} is colder than the observation (Climatic Research Unit TS data set version 4.01) by 0.62°C over the land (I. Harris et al., 2014), and colder than the ERA-Interim reanalyzes (European Center for Medium Range Weather Forecasting Re-Analysis Interim) by 0.30°C over the ocean (Dee et al., 2011). Hence T_{air} in the CM4-MG2 piControl ($12.78 \pm 0.14^{\circ}\text{C}$) is likely biased cold by 0.58°C or more (Figure 1d). One reason for the temperature cold bias is the snow-covered glacial albedo that has been purposely tuned higher during the CM4.0 development, in order to encourage the formation of Antarctic bottom water (Held et al., 2019).

3.2. Historical Experiments

3.2.1. Atmosphere Climatology

We evaluate the modeled atmosphere climatology over the period of 1980–2014. Three ensemble members of CM4-MG2 historical experiment are examined and compared to the CM4.0 counterpart experiment.

Figure 2a exhibits the global map of annual mean water vapor path (WVP) from three CM4-MG2 historical ensemble mean over 1980–2014. The observational reference is the NASA Water Vapor Project (NVAP) data set (Vonder Haar et al., 2012) in Figure 2b. CM4-MG2 shows high values of WVP over the tropics and oceans, and low values over land and toward high latitudes or polar regions. Both models underestimate WVP, especially over the equatorial Atlantic, Northern Africa, Southern Asia, Indian Ocean, and Antarctic. Compared to CM4.0, CM4-MG2 shows more water vapor, and larger WVP with a smaller global mean bias against the NVAP reference (-1.71 vs. -2.61 kg m^{-2}) (Figures 2c and 2d).

Figures 3a and 3b display the model biases of annual mean net downward shortwave flux or shortwave absorption (SWABS) at TOA over 1980–2014, computed relative to the Clouds and the Earth's Radiant Energy System-Energy Balanced and Filled climatology Edition 4.1 (CERES-EBAF-Ed4.1) (Loeb et al., 2009, 2018). In CM4-MG2 and CM4.0, negative biases are seen in the sub-Saharan Africa, western Indian Ocean, western Pacific storm track regions, tropical Atlantic, and near the Arctic (north of $\sim 60^{\circ}\text{N}$). Positive biases occur in the Southern Ocean (south of 60°S) and equatorial Pacific, and along the west coasts of South America, Africa, and North America, suggesting a lack of cloudiness. The lack of subtropical stratocumulus clouds off the west coasts have been a long-standing problem in the GFDL GCMs (Donner et al., 2011; Dunne, Horowitz, et al., 2020; M. Zhao et al., 2018a; Held et al., 2019).

This problem of coastal stratocumulus has improved noticeably with the introduction of the MG2 cloud microphysics in the AMIP mode simulations (Guo et al., 2021). More importantly, the fully coupled CM4-MG2 simulations successfully maintain this improvement, indicating that the enhanced subtropical stratocumulus is a robust feature when MG2 is active. This enhancement is related to the Seifert and Beheng (2001) autoconversion scheme and the prognostic precipitation treatment, which suppress the autoconversion of cloud water to rain at low liquid water paths and help sustain the subtropical stratocumulus. The improvement in the shortwave off the west coasts not only is a significant regional improvement, but also has important implications especially for coupled simulations. It helps reduce the warm SST biases of the underlying ocean, which will be discussed in Section 3.2.2.

Figures 3c and 3d provide the OLR biases at TOA, also computed relative to the CERES-EBAF-Ed4.1. Comparison of two model biases gives an overall improvement in root-mean-square-error in CM4-MG2 (RMSE, 5.75 vs. 6.31 W m^{-2} in CM4.0), and similar global mean bias (-2.19 vs. -2.37 W m^{-2} in CM4.0). Compared to the

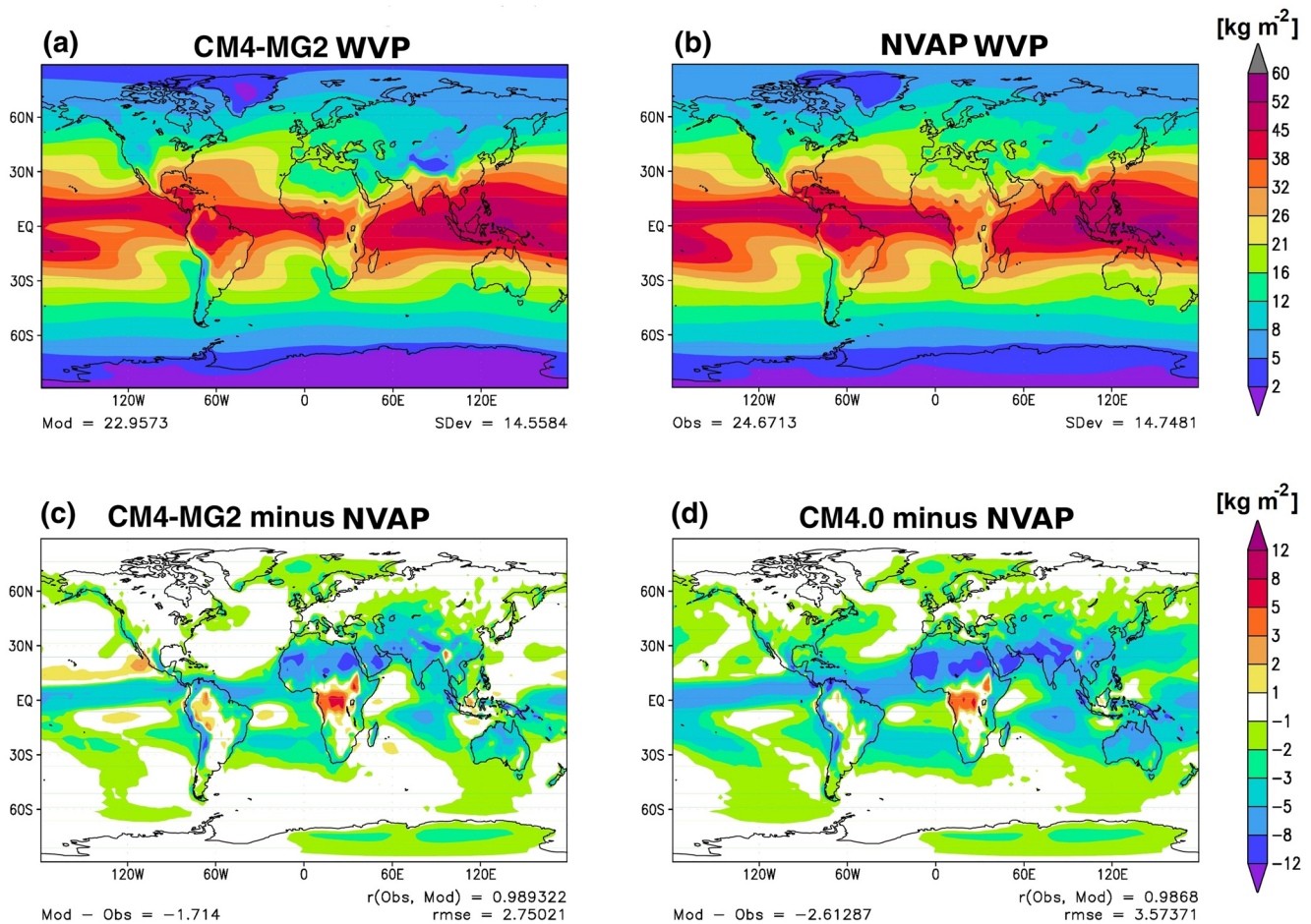


Figure 2. Annual mean column-integrated water vapor path (kg m^{-2}) from (a) three-member ensemble mean of CM4-MG2 over 1980–2014, (b) the NASA Water Vapor Project (NVAP) total column water vapor data sets (Vonder Haar et al., 2012), (c) CM4-MG2 model error (CM4-MG2 historical ensemble mean minus NVAP), and (d) CM4.0 model error.

AMIP (AM4-MG2 and AM4.0) simulations (Figures 4c and 4d in Guo et al., 2021), the RMSEs in CM4-MG2 and CM4.0 increase by about 30%–40%, as illustrated by stronger positive biases over the equatorial Pacific and Atlantic, and Amazon; and stronger negative biases over the Arctic. These positive biases are present where dry biases in precipitation are seen. The stronger negative biases over the Arctic are associated with the biases in SST and sea ice extent (SIE). The SSTs in CM4-MG2 and CM4.0 are biased cold and the sea ice extents are overestimated, which will be discussed in Section 3.2.2.

CM4-MG2 shows stronger negative SWABS and OLR biases than CM4.0 over the Arctic regions (Figure 3), suggesting excessive cloudiness. One reason is the atmosphere in CM4-MG2 is more humid (Figure 2), which favors more cloudiness since the large-scale cloud cover is parameterized as a function of relative humidity (Tiedtke, 1993). The global annual means and RMSEs of other radiative fields, for example, clear-sky SWABS (SWABS_clr) and OLR (OLR_clr) at TOA and shortwave and longwave radiative effect (SWCRE, LWCRE), are present in Table 2. CM4-MG2 shows lower OLR_clr and LWCRE than CM4.0 by about 1 W m^{-2} . Given more water vapor in CM4-MG2 (Figure 2), OLR_clr is effectively from the emissions at higher altitude (or colder temperature), and therefore lower.

Figures 4a and 4b exhibit the surface precipitation bias against Global Precipitation Climatology Project (GPCP) V2.3 (Adler et al., 2003, 2016). The global mean precipitation rates of CM4-MG2 and CM4.0 (2.85 vs. 2.89 mm day^{-1}) differ by 0.04 mm day^{-1} . The lower precipitation rate in CM4-MG2 is associated with precipitation efficiency, defined as the ratio of surface precipitation rate to the sum of column-integrated vapor condensation and deposition rates (Sui et al., 2005, 2007). The MG2 microphysics shows comparable

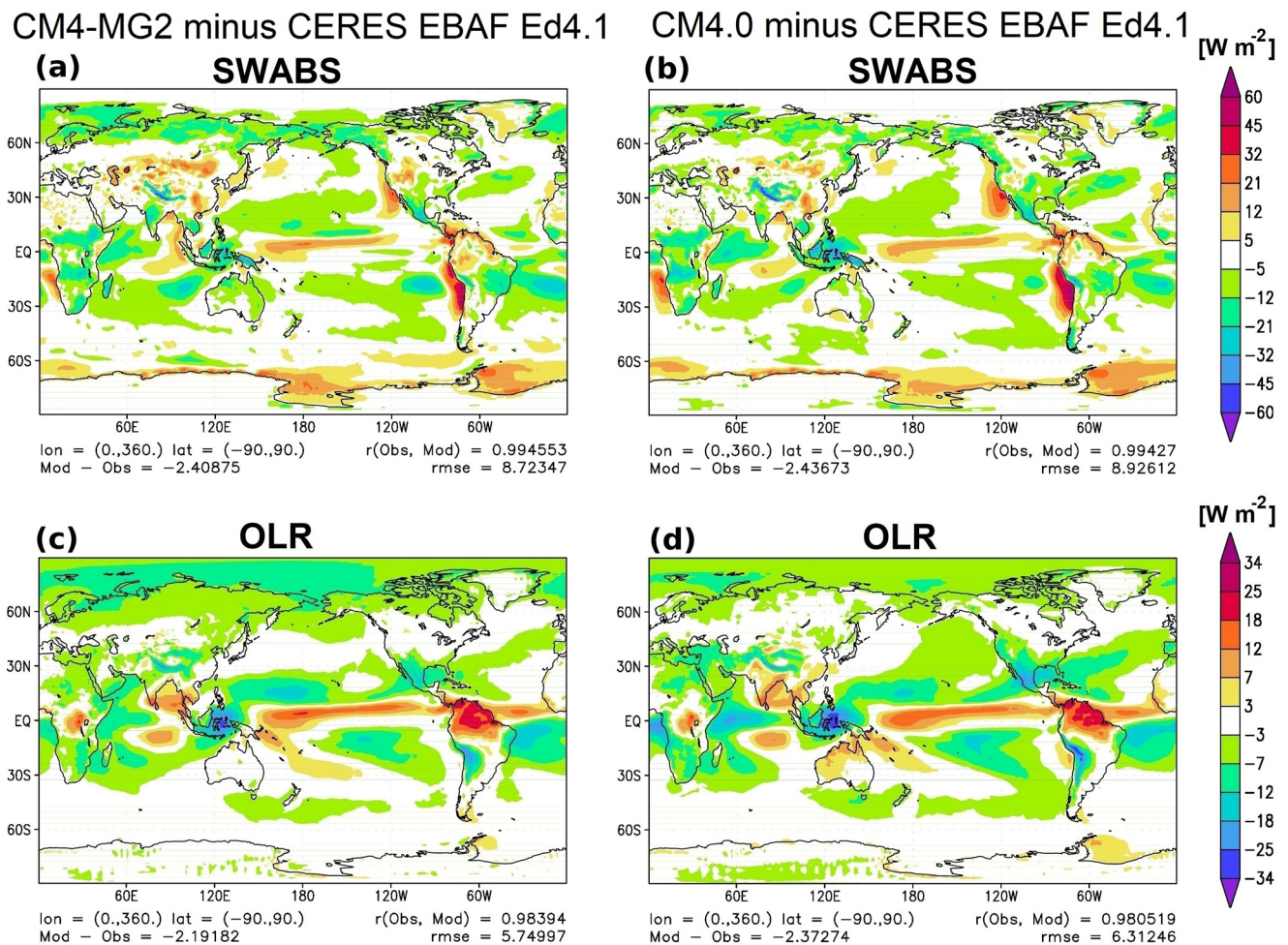


Figure 3. Model biases for three-member ensemble mean over 1980–2014 of annual-mean net downward shortwave flux or shortwave absorption (W m^{-2}) at top-of-atmosphere (TOA) in (a, b), and outgoing longwave radiation (W m^{-2}) at TOA in (c, d). The CM4-MG2 model biases are in (a, c), and the CM4.0 model biases are in (b, d). Observational reference is CERES–EBAF Ed4.1 (Loeb et al., 2009, 2018). Note that the CERES EBAF Ed4.1 observational data is averaged from 2000 to 2015 due to its unavailability prior to March 2000. Nevertheless, the specific averaging period is unimportant for these climatological averages.

condensation and deposition rates with the RK counterpart, but smaller large-scale surface precipitation rate by about 0.22 mm day^{-1} . Hence, the precipitation efficiency with MG2 is lower by about 10%. Because of the less efficient depletion of water vapor by precipitation, more vapor is present in CM4-MG2 (Figure 2).

Compared to the AMIP simulations (Figures 5c and 5d in Guo et al., 2021), CM4-MG2 and CM4.0 show reduced wet biases in Western Pacific, dry biases in Amazon and equatorial Pacific, as well as biases that often develop in coupled simulations: a wet maritime continent and a double ITCZ. Double ITCZ is a common bias persisting in a number of state-of-the-art fully coupled GCMs (Dunne, Horowitz, et al., 2020; Golaz et al., 2019; Held et al., 2019; Kelley et al., 2020; Voldoire et al., 2019). It is manifested as a zonal band of excessive precipitation across the Southern Hemisphere (SH) tropics at about 8°S . One notable achievement of CM4.0 is the reduced double ITCZ bias compared to GFDL's previous-generation GCMs (Held et al., 2019). It is encouraging that CM4-MG2 further reduces it, with smaller wet biases (less reddish) in the West Indian Ocean, the South Pacific Convergence Zone, and the tropical Atlantic Inter-Tropical Convergence Zone (Figures 4a and 4b). To highlight the ITCZ improvement, we compare the zonal mean precipitation over the eastern Pacific (90°W – 150°W). As shown in Figure 4c, the three CM4-MG2 ensemble members are closer to the GPCP observation over 2° – 10°S than the CM4.0 counterparts, indicating the reduced wet biases by this measure. By analyzing the precipitation partitioning, the reduced precipitation mainly come from smaller large-scale precipitation contribution. The annual mean large-scale precipitation rates over $[90^\circ\text{W}$ – 150°W , 2° – $10^\circ\text{S}]$ are 0.26 and 0.70 mm day^{-1} in CM4-MG2

Table 2

Global-Annual Means of Three Ensemble Members of CM4-MG2 and CM4.0 Historical Simulations for 1980–2014, and Observations: Shortwave Cloud Radiative Effect, Longwave Cloud Radiative Effect, Clear-Sky Shortwave Absorption (SWABS_clr), Clear-Sky Outgoing Longwave Radiation (OLR_clr) at Top-Of-Atmosphere Based on the CERES-EBAF (Loeb et al., 2018); Surface Latent Heat Flux (LH_flx), Surface Sensible Heat Fluxes (SH_flx), Surface Zonal Wind Stress (tau_x), Surface Meridional Wind Stress (tau_y), Sea Level Pressure in the Northern Hemisphere (SLP_NH), Sea Level Pressure in the Southern Hemisphere (SLP_SH) Based on the ERA-Interim Reanalyzes (Dee et al., 2011); Convective and Stratiform Liquid Water Path (LWP_{cw}) Over Ocean Based on the Multi-Sensor Advanced Climatology of Liquid Water Path (MAC-LWP) (Elsaesser et al., 2017); and Total Ice Water Path (IWP_{tot}) Based on the CloudSat (J. Jiang et al., 2012)

Variable	Observations	CM4-MG2	CM4.0
SWCRE (W m ⁻²)	45.39	−48.71 (9.28)	−48.74 (9.48)
LWCRE (W m ⁻²)	25.89	22.78 (5.32)	23.65 (5.18)
SWABS_clr (W m ⁻²)	286.93	287.37 (7.10)	287.38 (7.20)
OLR_clr (W m ⁻²)	268.22	260.80 (8.35)	261.48 (7.70)
LH_flx (W m ⁻²)	83.17	82.40 (9.45)	83.64 (9.48)
SH_flx (W m ⁻²)	17.48	18.49 (6.34)	18.22 (6.33)
tau_x (dPa)	0.12	0.08 (0.18)	0.09 (0.20)
tau_y (dPa)	0.02	0.004 (0.17)	0.002 (0.17)
SLP_NH (hPa)	1013.62	1013.16 (1.12)	1013.25 (1.00)
SLP_SH (hPa)	1009.02	1007.95 (2.57)	1007.72 (2.70)
LWP _{cw} ocean (g m ⁻²) ^a	81.06	80.53 (16.85)	60.50 (28.78)
IWP _{tot} (g m ⁻²) ^b	70.14	53.90 (39.78)	52.55 (40.73)

Note. Values in parenthesis indicate root-mean-square-errors (RMSEs).

^aLWP_{cw} includes both stratiform and convective cloud water, but not rain. ^bIWP_{tot} includes stratiform and convective cloud ice and snow.

and CM4.0, respectively, while their convective precipitation rates are close (1.37 vs. 1.31 mm day⁻¹). We also noticed a slight degradation in CM4-MG2 over the tropical Pacific around 2°–20°N. The degradation is associated with stronger convective precipitation, especially shallow convection. The convective precipitation over [150–240E, 2–20N] is about 0.69 mm day⁻¹ higher in CM4-MG2 than that in CM4.0.

Figure 5 illustrates the model biases of surface air temperature and relative humidity at 2 m, and surface zonal wind at 10 m compared to ERA-Interim (Dee et al., 2011). The simulated surface air temperature is biased cold, with a global mean value lower than the reanalysis by about 1.11 K. The cold bias partially arises from the boost of snow-covered glacial albedo, alleviating (or delaying) unrealistic superpolynya behavior in the Southern Ocean (Held et al., 2019). Albeit the cold bias is prevalent, the warm bias is present along the eastern boundaries of the subtropical ocean basins, as well as in the Ross Sea and the Weddell Sea. Relative to CM4.0, CM4-MG2 shows marked improvements along the eastern boundaries largely due to the enhanced subtropical stratocumulus, but moderate degradation in the Southern Ocean. Comparison of 2 m relative humidity reveals positive biases in both models, especially in the high latitudes (Figures 5c and 5d). CM4-MG2 shows larger biases there. We also noticed similar bias patterns in AMIP simulations with global mean biases of 4.09% in AM4-MG2 and 3.42% in AM4.0. One reason is less efficient precipitation formation and thus more humid atmosphere when MG2 is effective. This is consistent with higher WVP in CM4-MG2 (22.96 vs. 22.06 g m⁻² in CM4.0 as shown in Figure 2) and AM4-MG2 (24.51 vs. 23.63 g m⁻² in AM4.0). The surface zonal wind biases at 10 m in CM4-MG2 and CM4.0 exhibit similar geographical patterns: positive biases over the Antarctic and negative biases over the Indian Ocean and equatorial Pacific (Figures 5e and 5f). CM4-MG2 shows slightly larger global mean bias (−0.12 vs. −0.09 m s⁻¹ in CM4.0), but slightly smaller RMSE (0.63 vs. 0.67 m s⁻¹ in CM4.0). Additionally, Table 2 presents the global biases of surface wind stress (tau_x, tau_y), surface latent and sensible heat fluxes (LH_flx, SH_flx), and sea level pressure in the Northern and Southern Hemispheres (SLP_NH, SLP_SH). Both CM4-MG2 and CM4.0 show similar global means and RMSEs, and are close to the ERA-Interim reanalyzes with correlations of 0.90 or higher.

We further examine the annually and zonally averaged temperature and zonal wind biases (Figure 6). Both CM4-MG2 and CM4.0 share cold biases throughout the troposphere, consistent with the colder-than-observed SST discussed in Section 3.2.2. The cold bias is reduced in CM4-MG2 by about a factor of two in mid-upper troposphere over the tropical and mid-latitude regions, which is related to more water vapor there (Figure 2). The positive biases are present in the stratosphere in both models, but reduced in CM4-MG2. Consequently, the RMSE of the CM4-MG2's zonal mean temperature is smaller than that of CM4.0 (Figures 6a and 6b). For the zonal wind, both models underestimate the westerly throughout the midlatitude troposphere, and overestimate the trade winds in the tropics. Nevertheless the underestimate of the westerly and the overestimate of trade winds are ameliorated in CM4-MG2, leading to an overall smaller RMSE (1.05 vs. 1.36 m s⁻¹ in Figures 6c and 6d).

3.2.2. Ocean and Sea Ice Climatology

The SST biases, computed relative to the Hadley Center Sea Ice and Sea Surface Temperature (HadISST) data set over 1980–2014, averaged over three historical ensemble members for both CM4-MG2 and CM4.0 are displayed in Figure 7. The global mean biases (−0.64 vs. −0.63 K) and RMSEs (0.96 vs. 0.97 K) are comparable between CM4-MG2 and CM4.0. The geographical patterns of SST biases, to a large extent, are similar to surface air temperature biases (Figures 5a and 5b). There are prevailing cold biases in the subtropical highs and their poleward margins. The cold bias in the Western Pacific is reduced in CM4-MG2, partly due to moister surface air (Figures 5c and 5d) and thus smaller latent heat flux or weaker evaporative cooling there. Warm anomalies

Surface precipitation

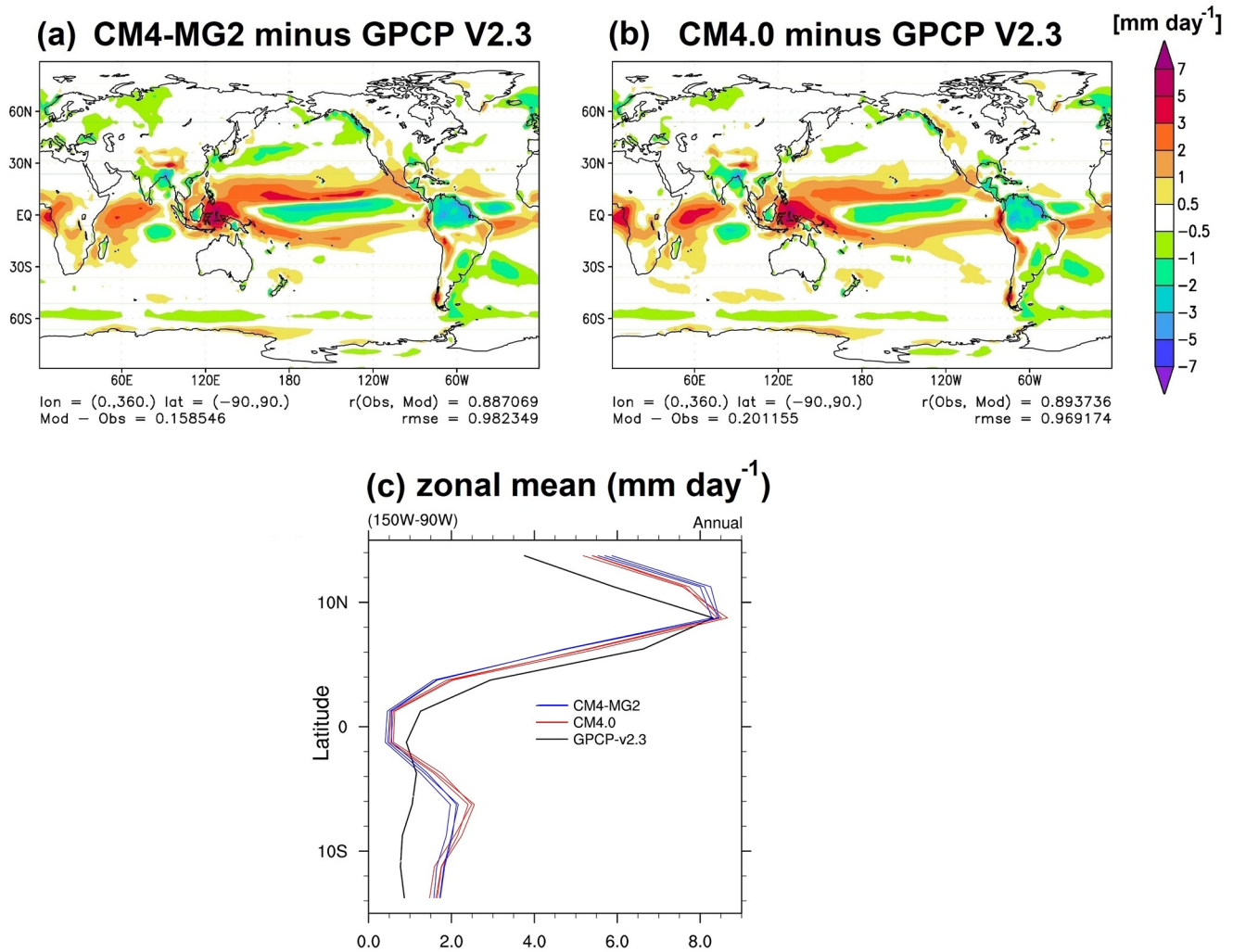


Figure 4. Model biases for three-member ensemble mean over 1980–2014 of surface precipitation (mm day^{-1}) in (a, b), and precipitation zonal means in (c). Observational reference is Global Precipitation Climatology Project V2.3 (Adler et al., 2003, 2016).

exist in the Northwest Atlantic Ocean and oceanic upwelling regions along the west coasts of Africa, North and South America. Due to the enhanced coastal stratocumulus clouds, the warm biases along the west coasts are (marginally) improved in CM4-MG2. But this improvement is less significant than what is found in the surface air temperature, suggesting that lack of subtropical stratocumulus clouds are only part of the reasons for the SST warm biases along the west coasts. Other factors, for example, insufficient ocean upwelling (Gent et al., 2010; Kuhlbrodt et al., 2018), are likely contributors, too.

The seasonal cycle of SIE is shown in Figure 8. Here the observational guidance is the passive microwave satellite observations from the National Snow and Ice Data Center (Cavalieri et al., 1996). Both models capture the amplitude and phase of the seasonal cycle of Pan-Arctic SIE, with maxima in March and minima in September. But both overestimate the SIE, and CM4-MG2 further amplifies it, especially during the boreal winter and summer. One reason is related to the cold SST bias (Figure 7). The cold SST favors sea ice formation and increases sea ice concentration and SIE. The overestimate of the Arctic sea ice is expected to enhance sea ice feedback, leading to higher climate sensitivity, which will be discussed in Section 3.5. Both CM4-MG2 and CM4.0 magnify the seasonal variation of Pan-Antarctic SIE, with positive biases in the austral winter and negative biases in the austral summer (Figure 8b). These Pan-Antarctic SIE biases are also present in the GFDL SPEAR (Seamless System for Prediction and Earth System Research) simulations (see their Figure 7b in Delworth et al., 2020). SPEAR is

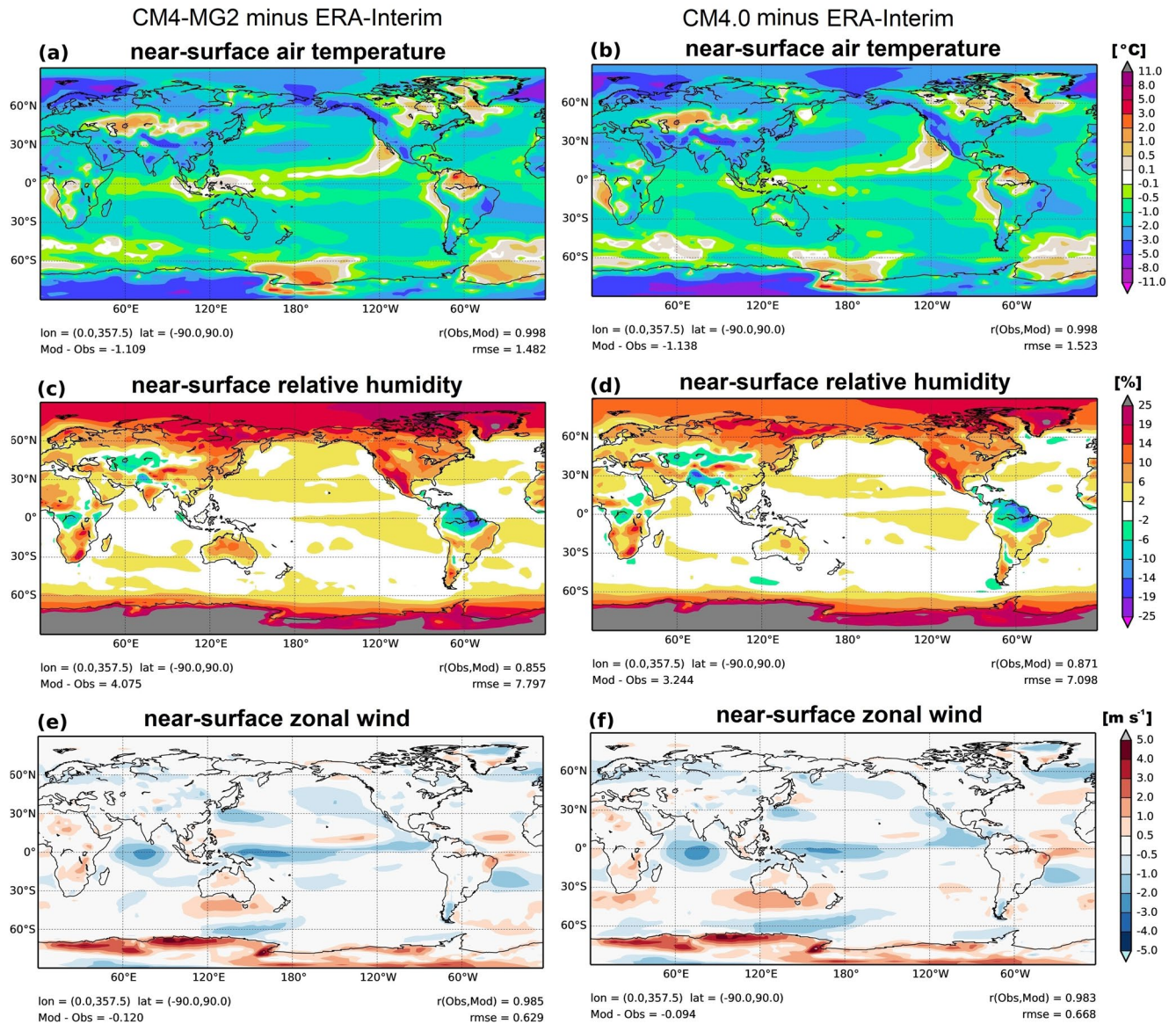


Figure 5. Model biases over 1980–2014 relative to ERA-Interim for near-surface (2 m) air temperature ($^{\circ}\text{C}$) in (a, b), near-surface (2 m) relative humidity (%) in (c, d), and near-surface (10 m) zonal wind (positive eastward, m s^{-1}) in (e, f).

GFDL's most recent generation modeling system for seasonal to multidecadal prediction and projection, with the capability of running large ensembles of simulations and ocean data assimilation. SPEAR shares the same atmosphere, land, ocean, and sea ice components with CM4.0, so it is not surprising that SPEAR and CM4.0 share the Pan-Antarctic SIE biases. These biases are associated with a positive SWABS bias at the surface during the austral summer season (December, January, February), especially over the Ross Sea and the Weddell Sea.

3.3. Climate Variability

The evaluations so far have been mainly focused on the mean model climate. In this section, we will assess the model performance from the climate variability perspective.

3.3.1. Madden–Julian Oscillation (MJO)

The Madden-Julian Oscillation (MJO) is a key climate variability mode (Madden & Julian, 1971, 1972). It is the largest component of the intraseasonal (30- to 90-day) variability and a key feature of moist convection in

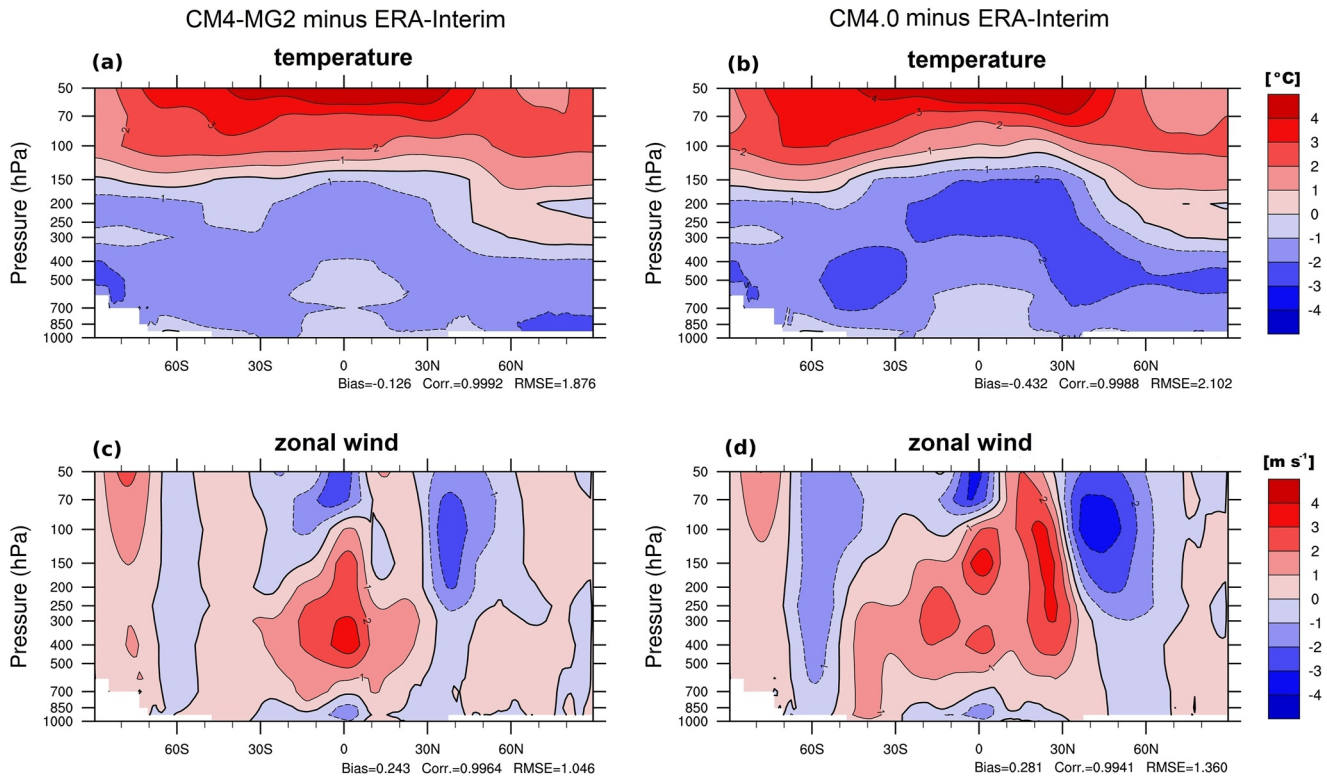


Figure 6. Annually and zonally averaged temperature ($^{\circ}\text{C}$) and zonal wind (m s^{-1}) biases relative to ERA-Interim from CM4-MG2 in (a, c) and from CM4.0 in (b, d), for three-member ensemble means over 1980–2014.

the tropical atmosphere. Recent studies have shown that lower tropospheric moisture and its advection play a key role for the propagation and magnitude of the MJO (Adames & Wallace, 2015; Benedict et al., 2014; X. Jiang, 2017; X. Jiang et al., 2020; H.-M. Kim, 2017; Pritchard & Bretherton, 2014). The atmospheric moisture has increased remarkably in CM4-MG2 (Figure 2). More moisture favors the development of convection in CM4-MG2 and CM4.0, due to the dependence of the lateral mixing rate of the deep plume on the free troposphere column relative humidity (see Equation 1 in Zhao et al., 2018b). The convective detrainment generally moistens the large-scale background. This is a positive feedback. Therefore it is expected that the MJO simulation will be impacted, even though the convection parameterization has not changed from CM4.0 to CM4-MG2.

Figure 9 shows the tropical symmetric power spectrum of OLR from 15°S to 15°N to assess the magnitude of MJO (Wheeler & Kiladis, 1999). The color shading regions indicate that the spectral power associated with MJO, Kelvin and other convective waves are greater than or equal to 1.2, which is above background noise. Obviously CM4-MG2 shows stronger tropical wave activity. For example, in zonal wave number 1–3 (or frequency $\sim 0.025 \text{ day}^{-1}$), there is enhanced MJO. CM4-MG2 shows stronger eastward propagating OLR signals than CM4.0, and thereby agrees better with the Advanced Very High Resolution Radiometer observation (Liebmann & Smith, 1996).

Further analyses are conducted by evaluating the life cycle of MJO. Figure 10 displays the composites of 20–100 day band-pass filtered daily anomalies in OLR and wind vector at 850 hPa (u_{850} , v_{850}) during the boreal winter season (November–April). The composites clearly illustrate the eastward propagation of convective signals, represented by the OLR anomalies. The negative OLR anomalies (associated with MJO) first develop over the Indian Ocean, get strengthened and pass through the Maritime Continent, then gradually decay and continue into the western Pacific. Both CM4-MG2 and CM4.0 well represent the traveling pattern of the MJO, compared to the ERA5 reanalysis. During the MJO life cycle, CM4-MG2 exhibits a larger magnitude of the OLR anomalies and/or stronger convective signals than CM4.0, and shows notable improvements in simulating the eastward propagation of the MJO.

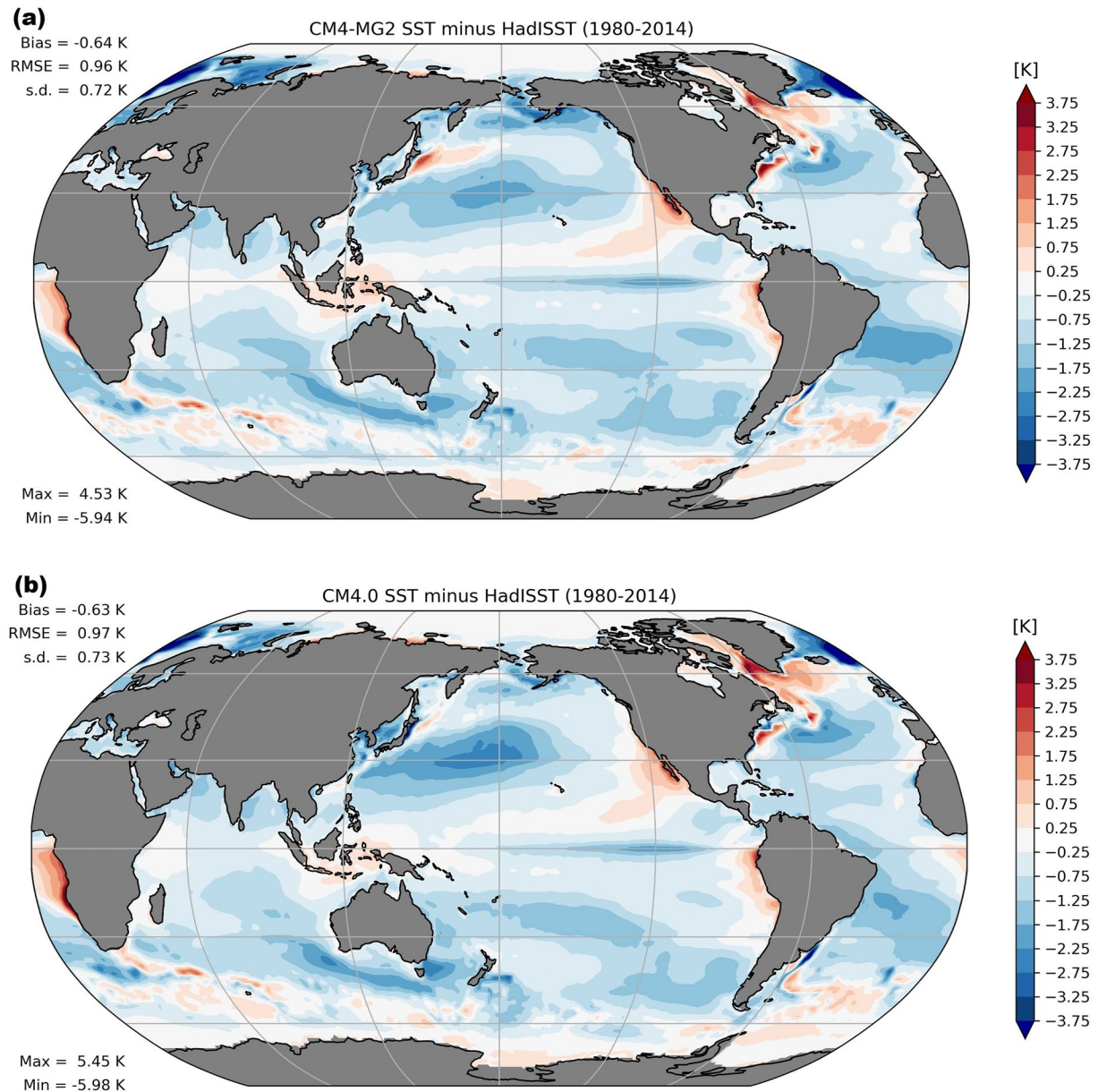


Figure 7. Sea surface temperature biases (K) in CM4-MG2 (a) and CM4.0 (b), from three historical ensemble members over 1980–2014, relative to the Hadley Center Sea Ice and Sea Surface Temperature data set (Rayner et al., 2003) for the same time period.

3.3.2. El Niño-Southern Oscillation (ENSO)

The El Niño-Southern Oscillation (ENSO) is Earth's strongest year-to-year climate fluctuation, involving SST variations in the tropical Pacific that have major impacts on the global climate system (McPhaden et al., 2020). Thus it is critical for climate models to simulate realistic ENSO variability.

We conducted wavelet analyses (Torrence & Compo, 1998) for SST averaged over the Niño-3 region [150°–90°W, 5°S–5°N], comparing the power spectra from observational reconstructions against those from the CM4-MG2 and CM4.0 piControl and historical ensemble (Figure 11). The observed spectrum, based on the National Oceanic and Atmospheric Administration (NOAA) Extended Reconstructed Sea Surface Temperature, version 5 observational reanalysis (Huang et al., 2017), shows a strong annual peak and a broad interannual peak spanning 2–8 years (W. S. Kessler, 2002; Larkin & Harrison, 2002; Wittenberg, 2009; Wittenberg et al., 2014). For CM4.0, the simulated spectra closely resemble the observations, with a broad interannual peak. For CM4-MG2, the spectra

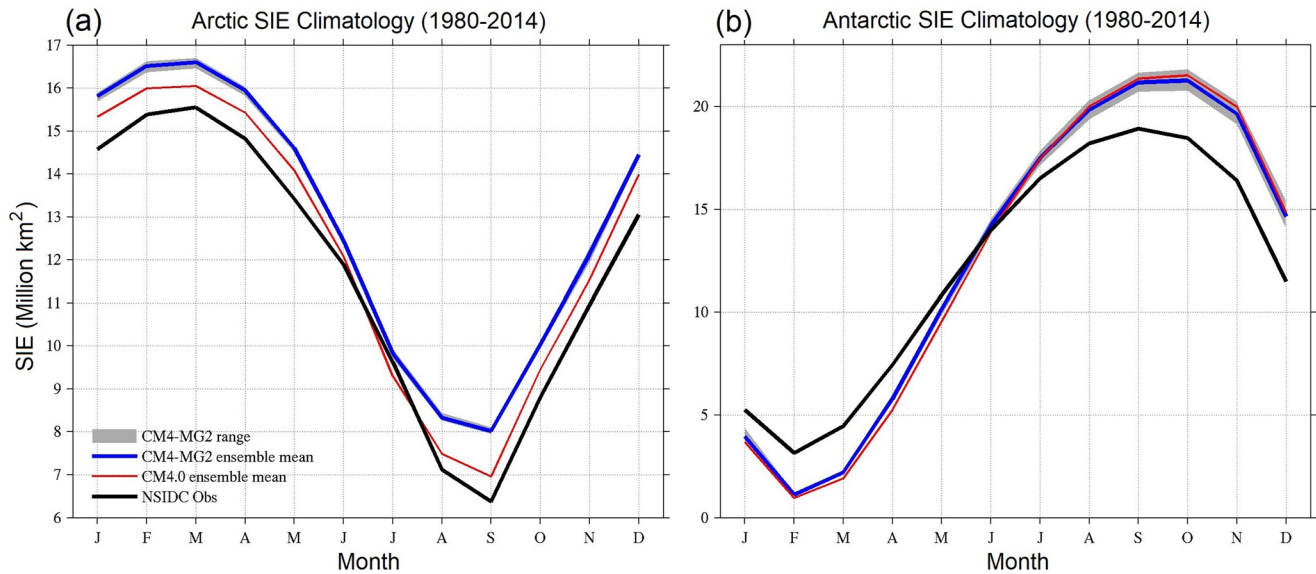


Figure 8. Sea ice extent (SIE) monthly climatologies (million km²) for Pan-Arctic in (a) and Pan-Antarctic in (b) from three CM4-MG2 historical ensemble mean (thick blue), the spread based on the minimum and maximum values of three CM4-MG2 ensemble members (gray shaded), three CM4-MG2 historical ensemble mean (thin red), and satellite observations (black) from the National Snow and Ice Data Center (Cavalieri et al., 1996). Pan-Arctic and Pan-Antarctic SIE are defined as the areal sum of all grid points whose sea ice concentration exceeds 15% in the Northern and Southern Hemispheres, respectively.

show a stronger ENSO with a somewhat longer period than observed. The ENSO period peaks near 3.5–4.0 years for CM4-MG2, while it is 3.3 years for observations and CM4.0. In both CM4.0 and CM4-MG2, the simulated historical annual cycle of Niño-3 SST is slightly stronger than observed; and moving from pre-industrial to historical forcings, the ENSO strengthens while the annual cycle weakens in both models. Given the excellent spectra in the CM4.0 historical simulations, it is somewhat disappointing that the enhanced subtropical stratocumulus in CM4-MG2 results in an apparent overestimate of the ENSO amplitude. Yet given the numerous competing coupled feedbacks involved in ENSO, it is often the case that improvements in one model component can unmask shortcomings in other components (Guilyardi et al., 2020; Wittenberg et al., 2018). These shortcomings need to be identified and addressed via additional iterations of coupled model development.

3.3.3. Atlantic Meridional Overturning Circulation (AMOC)

Figure 12 shows the maximum Atlantic Meridional Overturning Circulation (AMOC) at 26°N, which was estimated by integrating volume transport down from the ocean surface. The mean AMOC strengths, from the three CM4-MG2 and CM4.0 historical ensemble members over the period of 2004–2014, are about 16.38 and 15.82 Sv, which are close to the direct observation from the RAPID array ($\sim 16.9 \pm 3.35$ Sv) (Moat et al., 2020). In the historical simulations, the modeled AMOC exhibits a strengthening trend from 1940 to 1980, but after peaking around 1980, it shows a weakening trend (Figure 12a). These trends are generally consistent with the simulated AMOC variations in the state-of-the-art GCMs from CMIP6 (Hassan et al., 2021; Menary et al., 2020), and are related to the compensating effects between aerosols and greenhouse gases (GHGs) (Delworth & Dixon, 2006; Hassan et al., 2021; Menary et al., 2020). Increasing GHGs contributes to the weakening of the AMOC, while aerosols impose opposite effects and offset the GHG-induced weakening. The build-up of anthropogenic aerosols increases the strength of AMOC prior to 1980, and the following AMOC weakening stems from the reduced aerosol emissions and increasing GHGs.

Figure 12b provides the time series of the 10-year running average AMOC from the piControl simulations. The mean AMOC strengths from both models are comparable to the observed mean, with slightly stronger AMOC in CM4-MG2 than CM4.0 (17.26 vs. 16.71 Sv). But the multidecadal variability of the modeled AMOC is underestimated, evidenced by lower standard deviations of 0.54 Sv for CM4-MG2 and 0.60 Sv for CM4.0, versus 1.37 Sv for indirectly inferred observations (Yan et al., 2018). Furthermore, the simulated forced multidecadal AMOC variations (Figure 12a) are opposite to the historical multidecadal AMOC variations inferred from the observed AMOC fingerprints (i.e., a negative phase during 1970s and 1980s and a positive phase during 1960s

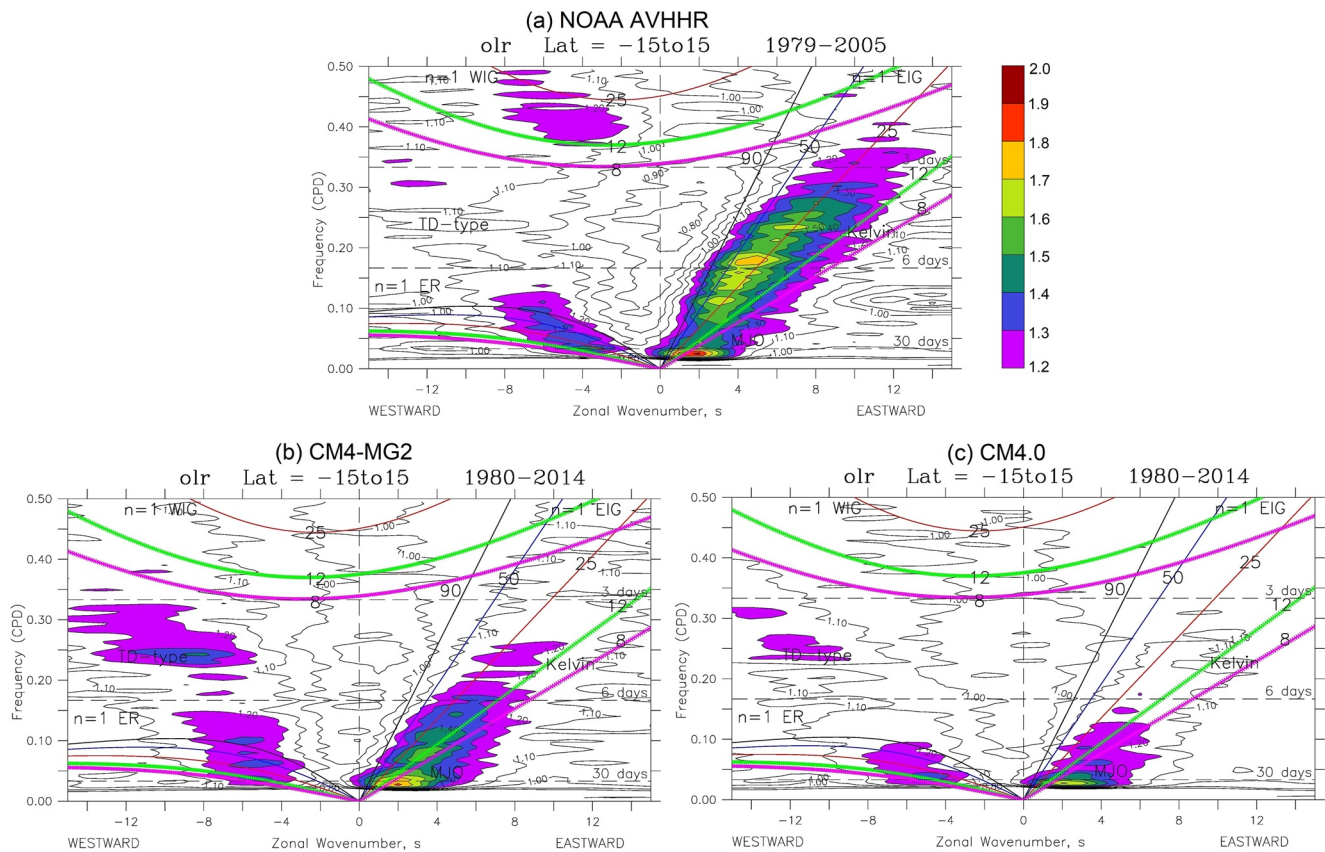


Figure 9. Normalized tropical (15°S – 15°N) symmetric power spectra of daily outgoing longwave radiation: zonal wavenumber versus frequency from (a) National Oceanic and Atmospheric Administration Advanced Very High Resolution Radiometer observation, (b) CM4-MG2, and (c) CM4.0. Note that color shading regions of greater than or equal to 1.2 indicate that spectrum power associated Madden-Julian Oscillation, Kelvin, and other convective waves are significant (above background noise). The black, blue, red, green, and purple lines are the dispersion curves of equatorial waves labeled for the five equivalent depths of 8, 12, 25, 50, and 90 m, respectively.

and post-1990), which are more likely dominated by internal variability (Yan et al., 2019). This discrepancy with the observational records is consistent with the muted internal multidecadal AMOC variability in this model. The lower multidecadal variability is associated with the buoyancy forcing (W. M. Kim et al., 2017), and is also partially related to the wind forcing (Yan et al., 2018; J. Zhao & Johns, 2014). Recent reconstructions of the long-term mean AMOC structure suggests that the Arctic is the northern terminus of the mean AMOC (Zhang & Thomas, 2021), and the simulated lower multidecadal AMOC variability is likely related to the underestimated multidecadal Arctic salinity variations in climate models due to the model biases in the Arctic (Rosenblum et al., 2021). Nevertheless, detailed discussion on the underlying reasons for the muted multidecadal AMOC variability is beyond the scope of this study.

3.4. Temperature Evolution and Aerosol Radiative Forcing

Figure 13a provides the time evolution (1850–2014) of the global mean surface temperature anomaly from the CM4-MG2 and CM4.0 historical ensembles, as well as the comparison against the observational estimate: NASA Goddard Institute for Space Studies Surface Temperature product version 4 (GISTEMP v4) (GISTEMP-Team, 2019; Lenssen et al., 2019). The temperature anomaly is the 5-year running average relative to the 1880–1900 period, which is the first 20-year of the GISTEMP data. From 1880 to 2014, the overall bulk global warming from both models agrees well with observations, although warmer than the observation before 1940 and colder after 1960. The cold bias persists until 2010 when it is virtually canceled out by the abrupt warming starting around 1990.

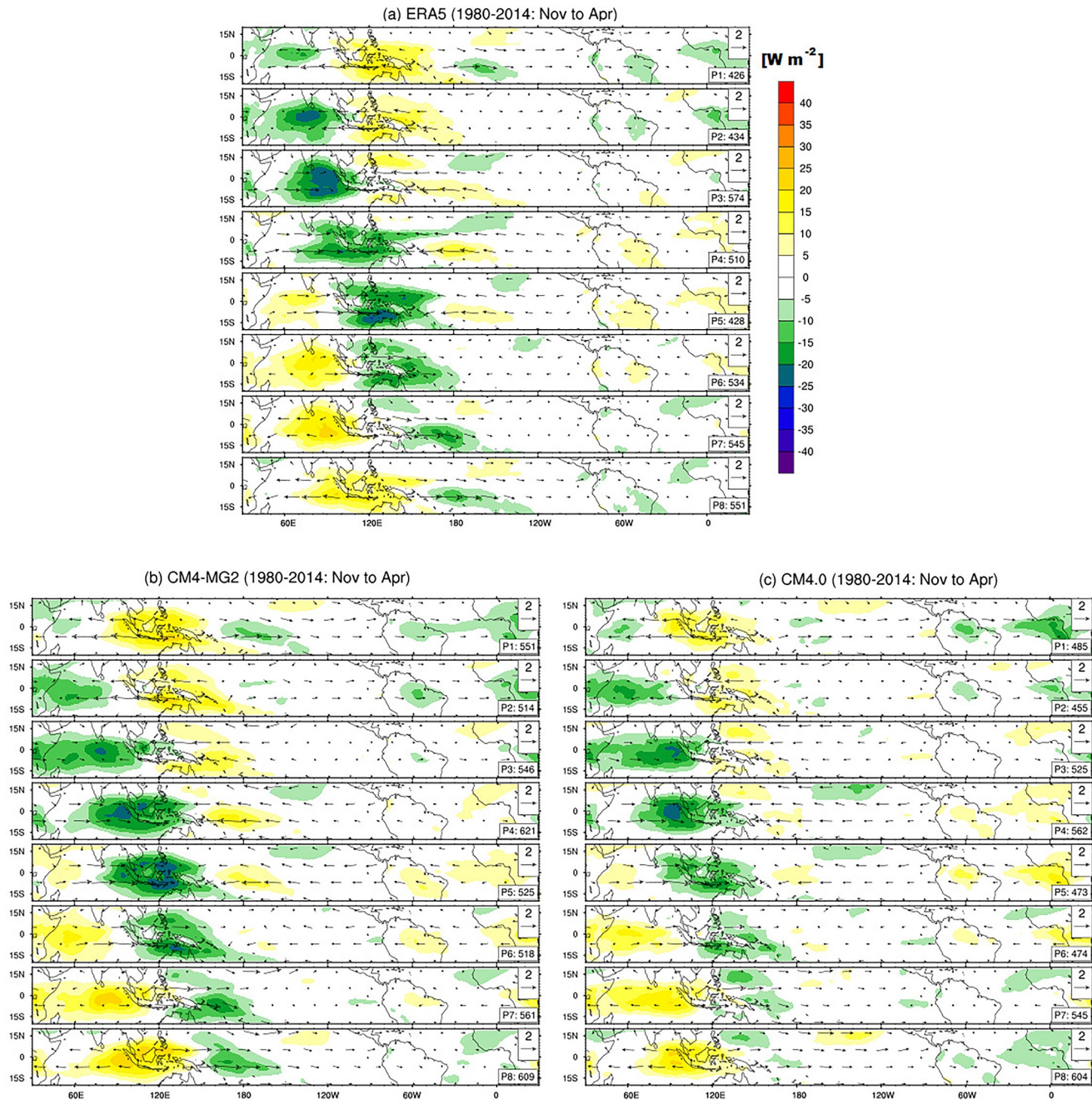


Figure 10. Composites of daily anomalies in outgoing longwave radiation (color shaded) and wind vector at 850 hPa (u_{850} , v_{850}) using 20–100 day band-pass filtered data during boreal winter season (November–April) for ERA5 in (a), CM4-MG2 in (b), and CM4.0 in (c).

More details about the warming are displayed in the difference of temperature anomaly between the Northern Hemisphere (NH) and the SH (Figure 13b). From 1920 to about 1980, the NH exhibits stronger warming than the SH from the GISTEMP observation, but neither CM4-MG2 nor CM4.0 captures this hemispheric warming asymmetry, indicating insufficient modeled warming in the NH, or excessive warming in the SH, or both (Held et al., 2019). The warming asymmetry is related to hemispheric asymmetry of aerosol forcing (C. Wang et al., 2021). After 1980, both models, especially CM4.0, show a rapid warming trend in the NH, similar to the abrupt warming in the global mean temperature since 1990 (Figure 13a). The rapid warming trend is related to aerosol radiative effect and climate sensitivity.

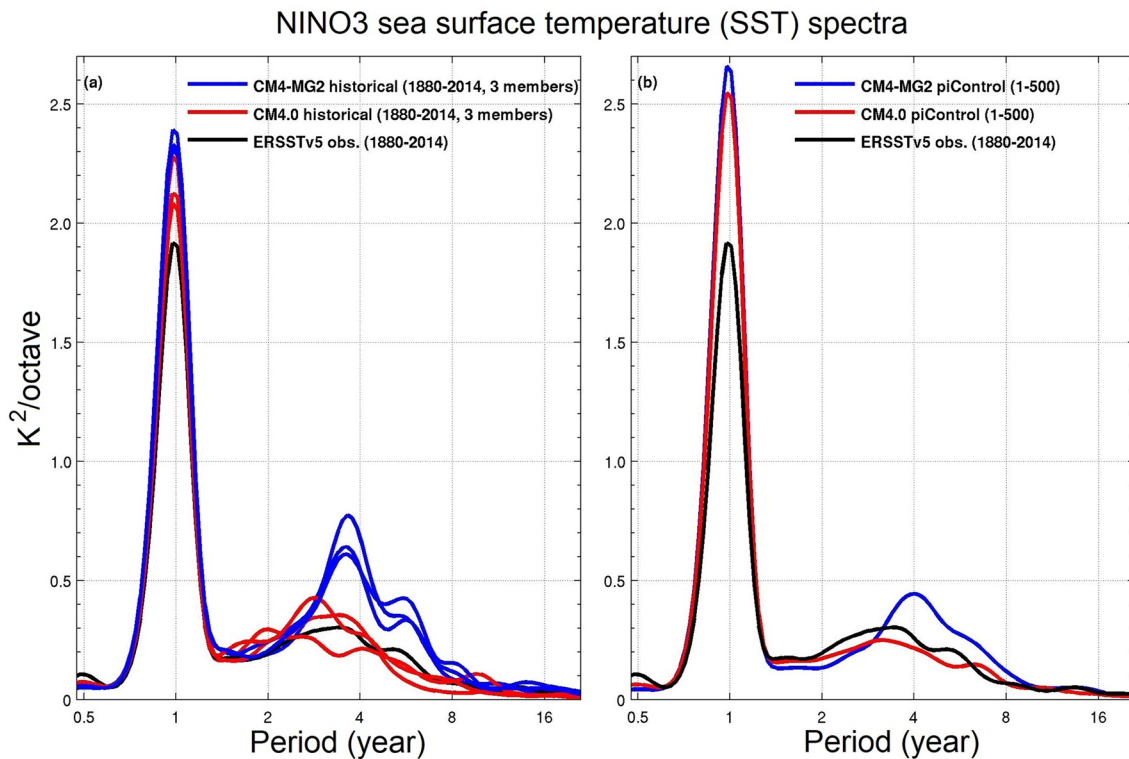


Figure 11. Wavelet power spectra of sea surface temperature averaged over the Niño-3 region [150–90°W, 5°S–5°N], following Figure 2 of Wittenberg (2009). Black curve is the 1880–2014 time-mean spectrum of the Extended Reconstructed Sea Surface Temperature, version 5 reanalysis (Huang et al., 2017); Colored curves in (a) are the 1880–2014 time-mean spectra for the three CM4-MG2 historical ensemble members (blue), and for the three CM4.0 ensemble members (red). Colored curves in (b) are the time-mean spectra for the corresponding 500-year piControl simulations.

The time series of aerosol radiative flux perturbation (RFPs) for the NH and the SH are shown in Figure 14. The RFP is estimated as the change in the TOA net radiation from a pair of AMIP simulations with identical SST and sea ice but different (present-day or pre-industrial) radiative forcing agents and their precursors (Forster et al., 2016; Golaz et al., 2011; Hansen et al., 2014; Lohmann et al., 2010). Here we conducted a pair of 145-year (1870–2014) AMIP runs with time-dependent or pre-industrial (1850) aerosol emissions, but non-aerosol forcing agents/precursors are time evolving. As anthropogenic aerosol emissions increase remarkably from 1920 to 1990, the aerosol RFP gets stronger (more negative) especially in the NH. During the period of 1970–1990, the RFP in the NH reaches -1.41 W m^{-2} and -1.65 W m^{-2} for CM4-MG2 and CM4.0, respectively. Such strong aerosol cooling is capable of offsetting or partially offsetting the greenhouse warming. After 1990, the aerosol RFP declines quickly (or becomes less negative) especially for CM4.0. The quick decline in the aerosol cooling, along with the rapid increase in the greenhouse warming, leads to an abrupt warming trend as shown in Figure 13. In addition to the aerosol radiative effect, climate sensitivity is another important factor influencing the global warming, which will be discussed in Section 3.5.

3.5. Climate Sensitivity and Cloud Feedback

Two idealized CO_2 forcing simulations: CO_2 concentration increasing 1% per year (1pct CO_2) and abruptly quadrupled CO_2 (abrupt-4x CO_2) (see Table 1), were conducted to evaluate climate sensitivity. Climate sensitivity is an important metric to understand the trajectory of the 20th century warming (Figure 13), as well as the long-term climate outcomes of the 21st century and beyond. For given anthropogenic forcing, a model with a higher climate sensitivity usually yields a larger temperature change.

Transient Climate Response (TCR) is a primary measure of climate sensitivity under increasing CO_2 scenario, referring to the warming at the time of CO_2 doubling (around Year 70) in the 1pct CO_2 experiment (Table 3). Figure 15a illustrates the time evolution of global annual mean surface air temperature change (ΔT). In response

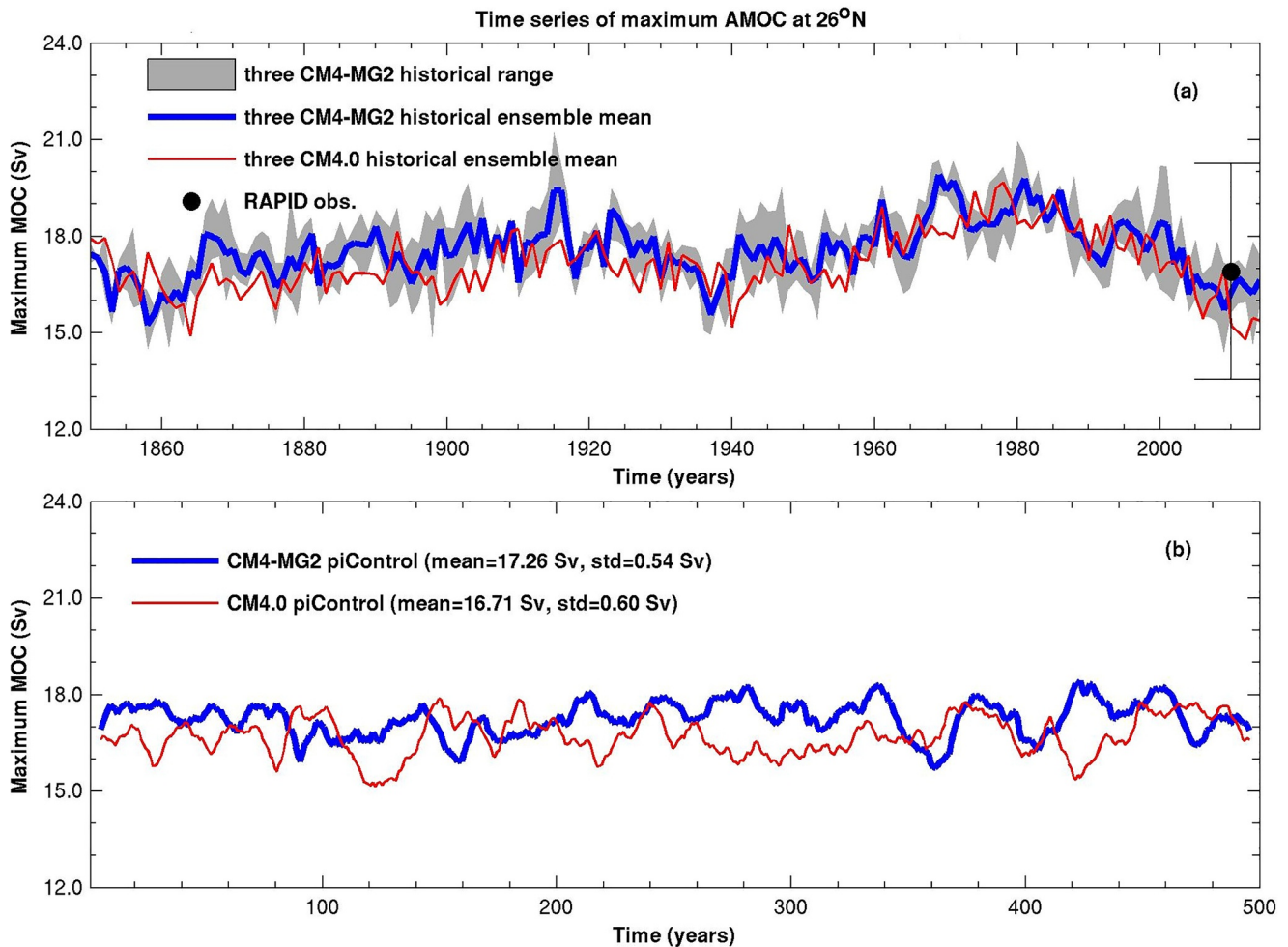


Figure 12. Time evolution of maximum Atlantic Meridional Overturning Circulation at 26°N from three CM4-MG2 historical ensemble mean (thick blue), the spread based on the minimum and maximum values of three CM4-MG2 ensemble members (gray shaded), three CM4.0 historical ensemble mean (thin red), and the RAPID array measurement over the period 2004–2015 in (a), and from CM4-MG2 and CM4.0 piControl experiments in (b).

to increasing CO₂ concentration, CM4-MG2 warms less than CM4.0. The TCR, from the difference of 20-year averages (i.e., Year 61–80) between the 1pctCO₂ and piControl, is about 10% lower in CM4-MG2 than that in CM4.0 (1.85 vs. 2.05 K). In Year 140 when CO₂ is quadrupled, the warming is about 4.16 K in CM4-MG2 but reaches 5.10 K in CM4.0, although both well above twice their corresponding TCRs. Furthermore, CM4-MG2 exhibits weaker warming than CM4.0 in the abrupt-4xCO₂ experiment (Figure 15b), echoing the less warming shown in the 1pctCO₂ experiments. The weaker warming in CM4-MG2 is related to a slower low-level cloud amount decrease as the climate warms, which reflects more sunlight back to space and exerts a cooling effect. This will be discussed in more detail later in this Section.

Another benchmark sensitivity metrics is equilibrium climate sensitivity (ECS), defined as the equilibrium global surface temperature change in response to CO₂ doubling. The evaluation of ECS is usually expensive computationally, because it takes thousands of model years for a coupled GCM to achieve equilibrium or steady state. As shown in Figure 15b, the 150-year simulation of the abrupt-4xCO₂ is far from equilibrium. Nevertheless, Winton et al. (2020) extended the abrupt-4xCO₂ experiment to 300 years and yielded an estimate of ECS of about 5.0 K for CM4.0. Following Dunne, Winton, et al. (2020), we estimated the ECS of 4.52 and 4.89 K for CM4-MG2 and CM4.0, respectively. Another comparable and widely used alternative is effective climate sensitivity (EffCS), following the method of J. Gregory et al. (2004). This method is to simply regress the TOA net radiative flux change (ΔN) against ΔT . From the linear regression for all 150 years of the abrupt-4xCO₂ experiment, EffCS can be diagnosed as the half of the ΔT -axis intercept (i.e., half of x -axis intercept in Figure 15c). The half is to

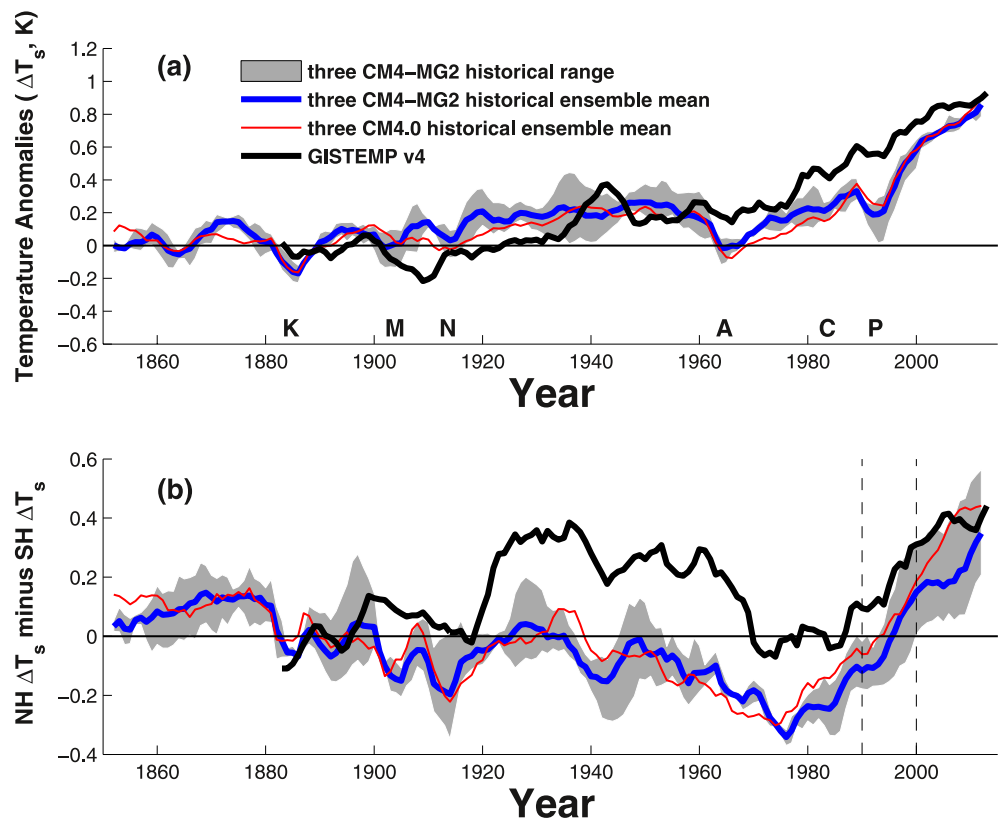


Figure 13. Time series of surface air temperature over land/sea ice and sea surface temperature over open ocean anomalies (ΔT_s , K) from 1880 to 2000 (a) for the globe, and (b) for the inter-hemispheric contrast between the Northern Hemisphere and Southern Hemisphere. A 5-year running average is applied to the model results and observations. The observations (black curve) are from the NASA Goddard Institute for Space Studies Surface Temperature product version 4 (GISTEMP-Team, 2019; Lenssen et al., 2019). Blue curve is the CM4-MG2 three historical ensemble mean, and the shaded region is the ensemble range. Red curve is the CM4.0 three historical ensemble mean. Letters above the horizontal axis mark major volcanic eruptions: Krakatoa (k) in 1883, Santa María (M) in 1902, Novarupta (N) in 1912, Agung (a) in 1963, El Chichón (c) in 1982, and Pinatubo (P) in 1991. Each eruption results in a dip in temperature.

evaluate EffCS with respect to a CO_2 doubling according to its definition. With this method, the estimates of EffCS are 3.31 and 3.91 K in CM4-MG2 and CM4.0, respectively. CM4-MG2's lower EffCS is consistent with its lower TCR. Apparently, the introduction of the MG2 cloud microphysics reduces the climate sensitivity.

In order to understand why the climate sensitivity is reduced, we diagnose effective radiative forcing from a doubling of CO_2 ($\text{Eff}F_{2x}$) and climate feedback parameter (λ_{net}) under the assumption of $\text{EffCS} = -\text{Eff}F_{2x}/\lambda_{\text{net}}$. Again $\text{Eff}F_{2x}$ and λ_{net} are derived by linear regression, and calculated as the half of the ΔN -axis intercept and the slope of the linear regression line (Figure 15c). We decompose ΔN into shortwave and longwave clear-sky, and cloud radiative effect (CRE) components. The CRE is defined as the net radiative flux difference between all-sky and clear-sky conditions. Using the same linear regression technique, we further decompose λ_{net} into shortwave clear-sky (λ_{SWclr}), longwave clear-sky (λ_{LWclr}), and cloud radiative effect (λ_{CRE}) feedback.

It is not surprising that lower EffCS in CM4-MG2 results from weaker $\text{Eff}F_{2x}$, and more importantly from smaller (more negative) λ_{net} (Table 3). This is similar to what is reported for the CMIP6 GCMs (as compared to the earlier CMIP5 generation GCMs). The combination of feedback and forcing results in higher EffCS in CMIP6: higher (less negative) feedback accounts for 60% increase of EffCS while stronger forcing only contributes to 20% increase (Zelinka et al., 2020). Hence λ_{net} is a major contributor to the change in EffCS.

The global map of λ_{net} is displayed in Figures 16b and 16c. The spatial patterns of λ_{net} are similar for CM4-MG2 and CM4.0. λ_{net} is mostly negative, and becomes positive in the North Asia, Northern Canada, tropical East Pacific, and Southern Ocean. The zonally averaged λ_{net} in CM4-MG2 is generally smaller (more negative) than

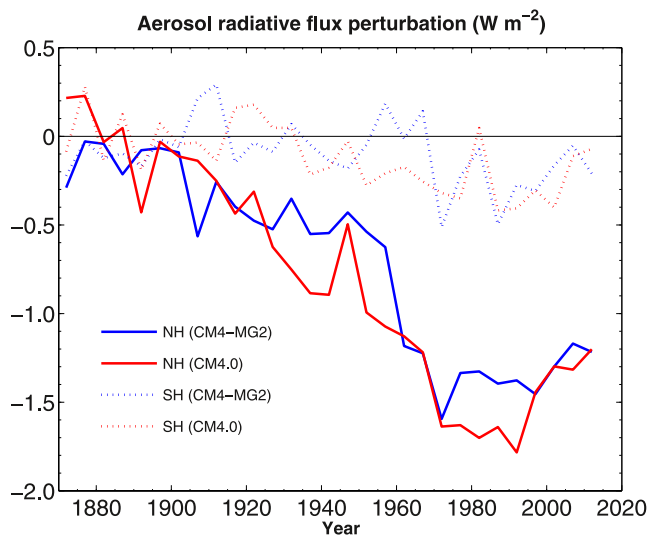


Figure 14. Time series of aerosol radiative flux perturbation (W m^{-2}) for CM4-MG2 (blue) and CM4.0 (red) in the Northern Hemisphere (solid) and Southern Hemisphere (dotted) derived from a pair of long Atmospheric Model Intercomparison Project simulations (1870–2014) with prescribed time-varying sea surface temperature and sea ice concentration. One simulation used the fixed aerosol emission levels at 1850 and the other simulation used the same forcing levels except for the time-varying aerosol emissions. Time series are computed by averaging over 5-year period.

(GFDL Global Atmosphere Model Development Team, 2004), whose radiation algorithm is consistent with what is adopted in CM4.0 and CM4-MG2. Compared to λ_{CRE} , λ_{CLD} is systematically more positive. Its global mean is enhanced by about $0.5 \text{ W m}^{-2} \text{ K}^{-1}$ (Table 3), similar to $\sim 0.3\text{--}0.4 \text{ W m}^{-2} \text{ K}^{-1}$ reported by Soden et al. (2004). The differences in λ_{CLD} between CM4-MG2 and CM4 mainly occur in the extratropics (e.g., poleward of 30°S) (Figures 17a–17c), and the global mean λ_{CLD} is reduced in CM4-MG2 (0.49 vs. $0.66 \text{ W m}^{-2} \text{ K}^{-1}$ in CM4.0). It is notable that given the approximations of the kernel technique, there often exists a residual feedback term, which is the difference between λ_{net} and the sum of kernel-derived components (Table 3). The residual term here is acceptably small ($\sim 0.1\text{--}0.2 \text{ W m}^{-2} \text{ K}^{-1}$). So cloud feedback results are not expected to change qualitatively.

In order to better understand the reduction in λ_{CLD} , we analyze low-level cloud amount and LWP changes against ΔT (Zelinka et al., 2020). The low-level cloud amount tends to decrease (positive feedback) while the LWP tends to increase (negative feedback) as the climate warms. Figures 17g–17i show the zonal average and geographic distribution of the LWP change. CM4-MG2 exhibits stronger LWP increase in the tropical west Pacific. One reason is associated with less efficient ice nucleation and thus more liquid clouds with warming. CM4-MG2 seems to experience weaker LWP increase in the extratropics (especially in the Southern Ocean) (Figures 17h and 17i). The weaker increase is related to higher liquid fraction (or more super-cooled water) in CM4-MG2 (Andrews et al., 2019; Zelinka et al., 2020). When MG2 and dust-dependent ice nucleation are active, the super-cooled liquid fraction tends to be higher for the mixed-phase clouds of temperature between -30° and -10°C (See Figure 11 in Guo et al. (2021)). The smaller LWP increase is supposed to reduce cooling, leading to weaker negative (or stronger positive) cloud feedback in CM4-MG2.

However, the LWP increase with warming is accompanied by low-level cloud amount decrease, consistent with what is reported in the AMIP mode simulations (M. Zhao et al., 2016). As shown in Figure 17d, both CM4-MG2 and CM4.0 exhibit reduced cloud amount with warming. But the cloud amount reduction is smaller in CM4-MG2 ($-1.62\% \text{ K}^{-1}$ vs. $-2.04\% \text{ K}^{-1}$ in CM4.0), leading to less positive cloud feedback. The net cloud feedback turns out to be $0.49 \text{ W m}^{-2} \text{ K}^{-1}$ in CM4-MG2, lower than $0.66 \text{ W m}^{-2} \text{ K}^{-1}$ in CM4.0 (Table 3). The decrease in low-level cloud amount is related to precipitation efficiency (M. Zhao et al., 2016). In order to explore the impacts of precipitation efficiency, we have conducted a pair of present-day simulation and global warming simulation with SST uniformly warmed by 2 K following Cess et al. (1990), and compared precipitation effi-

that in CM4.0, except for N. Subpolar region where λ_{net} peaks (Figure 16a). The larger λ_{net} around 70°N in CM4-MG2 is mainly because of λ_{SWclr} . As shown in Figures 16d–16f, λ_{SWclr} ranges from neutral to strongly positive. CM4-MG2 exhibits larger λ_{SWclr} , especially poleward of 60°N . We attribute the larger λ_{SWclr} mostly to the decrease of surface albedo due to changes in snow cover and SIE with warming in the Arctic. Both models overestimate the Arctic sea ice extent, but CM4-MG2 amplifies the overestimate (Figure 8a). This amplification further enhances the positive sea ice albedo feedback, and therefore increases the feedback in the Arctic. Note that the longwave clear-sky feedback (λ_{LWclr}) does not differ much between CM4-MG2 and CM4.0 (Table 3). So we will not discuss it further. The difference in λ_{net} largely stems from the differences in λ_{SWclr} and λ_{CRE} .

The positive λ_{SWclr} in the high-latitudes is partly balanced by the cloud radiative effect feedback (λ_{CRE}) (Figures 16g–16i). Both CM4-MG2 and CM4.0 show strong negative λ_{CRE} in the Arctic and Southern Ocean, counteracting the strong positive λ_{SWclr} . Although both models share similar spatial patterns, for example, noticeably bimodal distribution (i.e., negative peaks at poleward of about 60°S and 70°N), CM4-MG2 overall exhibits more negative λ_{CRE} (with the global mean decreasing from 0.18 to $-0.02 \text{ W m}^{-2} \text{ K}^{-1}$). Note that the differences in λ_{CRE} cannot be simply ascribed to the differences in clouds (or cloud feedback). Some changes in cloud radiative effect come from the cloud mask of clear sky fluxes, rather than from cloud changes. So λ_{CRE} does not truly represent cloud feedback (λ_{CLD}). In order to better account for cloud masking effects, we then estimate λ_{CLD} using the radiative kernels described in Soden et al. (2008), instead of the linear regression. These radiative kernels were estimated using a control integration of the GFDL AM2

Table 3
Global Mean CO₂ Effective Radiative Forcing, Sensitivity, and Feedback due to CO₂ Doubling

	CM4-MG2	CM4.0
TCR (K)	1.85	2.05
EffCS (K)	3.31	3.91
EffF _{2x} (W m ⁻²)	2.95	3.16
λ _{net} (W m ⁻² K ⁻¹)	-0.89	-0.81
λ _{SWclr} (W m ⁻² K ⁻¹)	0.95	0.81
λ _{LWclr} (W m ⁻² K ⁻¹)	-1.82	-1.80
λ _{CRE} (W m ⁻² K ⁻¹)	-0.02	0.18
λ _{SWCRE} (W m ⁻² K ⁻¹)	-0.20	-0.06
λ _{LWCRE} (W m ⁻² K ⁻¹)	0.18	0.24
λ _{CLD} (W m ⁻² K ⁻¹)	0.49	0.66
λ _{SWCLD} (W m ⁻² K ⁻¹)	-0.04	0.09
λ _{LWCLD} (W m ⁻² K ⁻¹)	0.53	0.57
λ _{albedo} (W m ⁻² K ⁻¹)	0.48	0.47
λ _{Planck} (W m ⁻² K ⁻¹)	-3.53	-3.55
λ _{LR} (W m ⁻² K ⁻¹)	-0.25	-0.20
λ _{vapor} (W m ⁻² K ⁻¹)	1.73	1.68
Cess feedback (W m ⁻² K ⁻¹)	-2.02	-1.77

Note. TCR (transient climate response) is global mean surface air temperature change (ΔT , K) at the time of doubled CO₂ (Year 70) in the 1pctCO2 experiment (Table 1), evaluated as a time-mean over years 61–80 (J. M. Gregory & Forster, 2008). EffCS, EffF_{2x}, and λ_{net} are the effective climate sensitivity, 2xCO₂ radiative forcing, and net climate feedback parameter, respectively. They are estimated from a linear regression of net radiative flux change (ΔN , W m⁻²) at top-of-atmosphere (TOA) against ΔT for all 150 years of the abrupt-4xCO2 experiment (Table 1). EffCS and EffF_{2x} are the ΔT -axis and ΔN -axis intercepts divided by 2; λ_{net} is the slope of the linear regression line. λ_{SWclr}, λ_{LWclr}, and λ_{CRE} are clear-sky shortwave, clear-sky longwave, and cloud radiative effect (CRE) feedback parameters. The total feedback is also decomposed into cloud (λ_{CLD}), surface albedo (λ_{albedo}), Planck (λ_{Planck}), lapse rate (λ_{LR}), and water vapor (λ_{vapor}) feedback components using the radiative kernels based on the GFDL AM2 model (Soden et al., 2008). The cloud feedback (λ_{CLD}) is further decomposed into shortwave (λ_{SWCLD}) and longwave (λ_{LWCLD}) cloud feedback. The Cess feedback is calculated as ΔN divided by the warming of sea surface temperature (SST) from a pair of present-day simulation and global warming simulation with SST uniformly increased by 2 K.

ciency changes in a warmer climate. The precipitation efficiency is calculated as the ratio of surface precipitation rate to the sum of column-integrated vapor condensation and deposition rates (Sui et al., 2005, 2007). It is found that clouds occur less frequently and precipitation efficiency decreases with warming. The precipitation efficiency is reduced by about 0.72% K⁻¹ with MG2, and by about 0.49% K⁻¹ with RK, respectively. The stronger reduction in precipitation efficiency with MG2 results in weaker decrease in the low cloud amount (see their Figure 4 in M. Zhao et al. (2016)), which contributes to less warming (or less positive cloud feedback). This is further supported by more negative Cess feedback when MG2 is active (-2.02 vs. -1.77 W m⁻² K⁻¹ in Table 3). Although recent studies showed that the Cess experiments provide useful insight on cloud feedback (Brient et al., 2015; Ringer et al., 2006, 2014), a caveat is that the Cess approach assumes uniform SST warming and ignores important feedbacks, such as sea ice feedback and polar amplification. Hence the Cess feedback might underestimate the feedback of high latitude processes. The impacts of precipitation efficiency on cloud feedback (or climate sensitivity) in the fully coupled mode need more research in the future.

4. Summary

This paper describes the model performance and simulation characteristics of a fully coupled atmosphere-ocean-land-sea ice model configuration: CM4-MG2, and comparisons to the base model: CM4.0. CM4-MG2 and CM4.0 share the same ocean, sea ice, and land components. They only differ in the atmospheric component, more specifically cloud microphysics: two-moment Morrison-Gottelman bulk microphysics with prognostic precipitation (MG2) versus partial two-moment RK bulk microphysics with diagnostic precipitation (RK), and the mineral dust and temperature-dependent ice nucleation scheme. Based on a suite of CMIP6 DECK and historical simulations, model mean climate, climate variability, the 20th century simulation, and climate sensitivity have been examined and evaluated against available observations and reanalyses.

The CM4-MG2 mean climate is similar or better relative to CM4.0 in terms of RMSE metrics. The achievements of CM4-MG2 include enhanced subtropical stratocumulus and reduced double ITCZ bias. The enhancement is a robust feature in both atmosphere-only and coupled simulations when MG2 is active. This is mainly attributed to the more realistic prognostic precipitation treatment and autoconversion parameterization (Guo et al., 2021). The enhanced stratocumulus also ameliorates the underlying SST warm bias along the west coasts of continents. The degradation is the overestimate of the Arctic sea ice extent.

The simulated climate variability generally compares favorably with observations. CM4-MG2 shows stronger eastward propagating MJO signals than CM4.0, and agrees better with observations and reanalyses. One plausible reason is that the atmosphere is more humid in CM4-MG2 due to lower precipitation efficiency of MG2. The improved MJO simulation is expected to benefit the sub-seasonal to seasonal prediction (Xiang et al., 2021). Compared to the credible ENSO simulation with CM4.0, CM4-MG2 overestimates the spectral power and period lengths of ENSO. The modeled mean AMOC strength is in good agreement with the direct observation of RAPID, although its variability is muted. Both CM4-MG2 and CM4.0 simulate a strengthening trend of AMOC from 1940 to 1980 and a compensating reduction thereafter, due to the compensating effects between aerosols and GHGs. However, these simulated forced multidecadal AMOC variations are opposite to those inferred from the observed AMOC fingerprints over the second half of the twentieth century, which show a negative phase during 1970s and 1980s and a positive phase during 1960s and post-1990 and are more likely dominated by

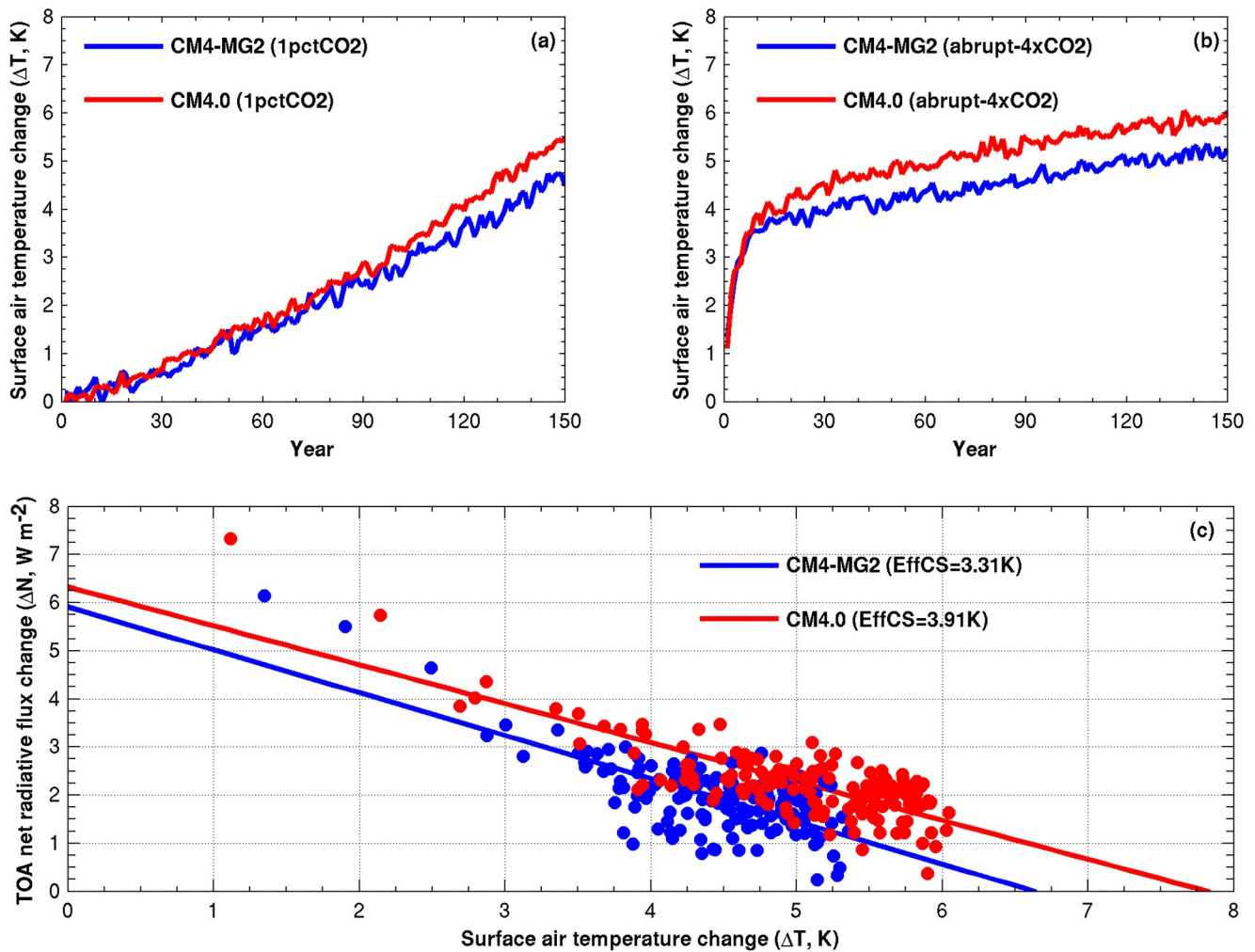


Figure 15. Time series of global annual mean surface air temperature change (ΔT , K) in the 1pctCO₂ (a) and abrupt-4xCO₂ (b) experiments relative to the pre-industrial control (piControl) experiment. (c) ΔT versus top-of-atmosphere net radiative flux change (ΔN , W m⁻²) of the abrupt-4xCO₂ relative to the piControl. Linear regressions are depicted with solid lines for CM4-MG2 (blue) and CM4.0 (red), respectively. The effective climate sensitivity is calculated as the half of the ΔT -axis intercept.

internal variability (Yan et al., 2019). This discrepancy between CM4.0/CM4-MG2 and the observational records is consistent with the fact that CM4.0/CM4-MG2 has insufficient internal multidecadal AMOC variability.

Both CM4-MG2 and CM4.0 are capable of simulating the bulk warming of the 20th century. But the temporal evolution of historical warming, to some extent, departs from the observation: insufficient warming from 1960 to 1990 and too rapid warming from then on. An analysis on the hemispheric warming asymmetry between the NH and SH reveals the cold bias (or insufficient warming) in the NH prior to 1980 and subsequently abrupt warming, especially in CM4.0. The abrupt warming and warming asymmetry are also concerns for a number of CMIP6 GCMs (Danabasoglu et al., 2020; Golaz et al., 2019; Held et al., 2019; C. Wang et al., 2021). The reasons are associated with aerosol radiative forcing and climate sensitivity (C. Wang et al., 2021). CM4-MG2 exhibits weaker (less negative) aerosol forcing than CM4.0 particularly in the NH, because the prognostic precipitation treatment in MG2 suppresses the dependency of rain formation on cloud drop size or number concentration (Gettelman et al., 2015b; Guo et al., 2021; Posselt & Lohmann, 2008, 2009).

CM4-MG2 exhibits lower climate sensitivity than CM4.0. The TCR is 1.85 and 2.05 K for CM4-MG2 and CM4.0, respectively. The effective climate sensitivity (ECS) is 3.31 and 3.91 K, which are well within the expert estimated range (2.3–4.7 K) (Sherwood et al., 2020). It is not surprising that lower sensitivity largely results from weaker cloud feedback (Andrews et al., 2012; Webb et al., 2006), especially shortwave component (C. Wang

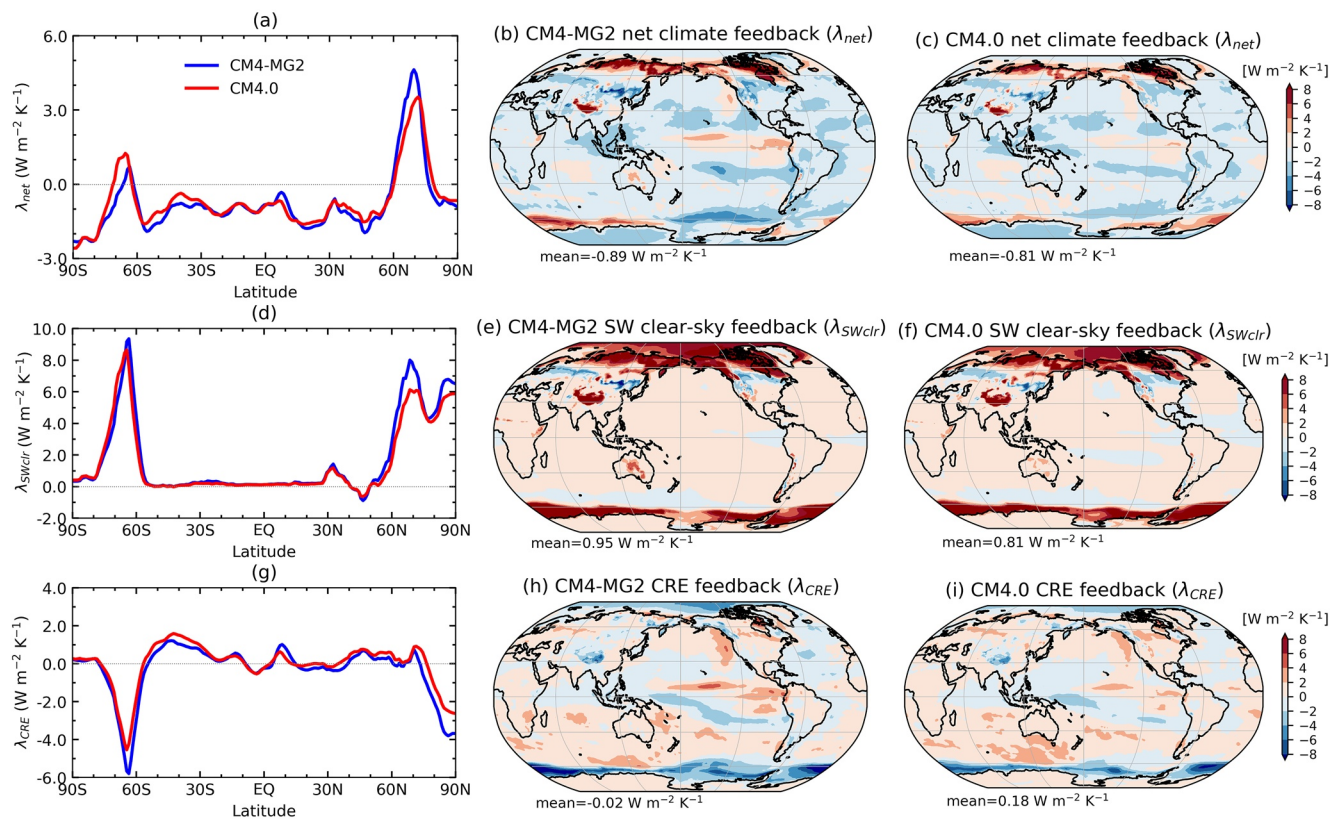


Figure 16. Zonal mean net climate feedback parameter (λ_{net} , $\text{W m}^{-2} \text{K}^{-1}$) in (a), and its shortwave clear-sky component (λ_{SWclr}) in (d) and cloud radiative effect (CRE) component (λ_{CRE}) in (g), and their geographical distributions from CM4-MG2 in (b, e, and h), and from CM4.0 in (c, f, and i). λ_{net} , λ_{SWclr} , and λ_{CRE} are calculated by linearly regressing the change in net radiative flux at top-of-atmosphere, and its shortwave clear-sky and CRE components against surface air temperature change (ΔT) for all 150 years of the abrupt-4xCO₂ simulations.

et al., 2021; Zelinka et al., 2020). We further analyzed the changes of LWP and low-level cloud amount, and found that when the climate warms, CM4-MG2 exhibits weaker LWP increase and weaker low cloud amount decrease than CM4.0, especially over the Southern Ocean. These changes are related to higher liquid fraction and stronger precipitation efficiency reduction with warming in CM4-MG2. As demonstrated by M. Zhao et al. (2016), precipitation efficiency could strongly affect the model estimate of Cess sensitivity in the AMIP mode. The lower climate sensitivity in CM4-MG2 is also partly associated with precipitation efficiency. A more detailed investigation on the impacts of precipitation efficiency in the coupled mode is beyond the scope of current paper and warrants further research.

The MG2 cloud microphysics is more expensive computationally than the RK scheme, mainly due to additional prognostic tracers (e.g., number and mass of rain and snow, ice crystal number concentration) and substepping in cloud microphysics. As a result, the overall computational cost increases by about 10% in the AMIP mode simulations (Guo et al., 2021). However, in the fully coupled simulations, there are barely any noticeable slow-down because of the loading balance between different model components. In the current configuration of CM4.0, the wall clock time for the ocean/sea ice component is slower than that of atmosphere/land component by 10% or more. This probably masks the slowdown caused by the MG2 microphysics in the CM4-MG2 atmospheric component.

While the CM4-MG2 coupled global simulations are promising, there are areas for further improvements and/or exploration. The MG2 microphysics enhances the subtropical stratocumulus clouds, but there is still lack of stratocumulus especially along the coasts, as shown by noticeable positive biases in the SWABS. Refined vertical resolution can better resolve sharp temperature and moisture gradients of inversion, and is expected to better represent subtropical boundary layer clouds (Bogenschutz et al., 2021; Lee et al., 2021). The trajectory of the 20th century warming and hemispheric warming asymmetry somewhat deviates from the observation. This could

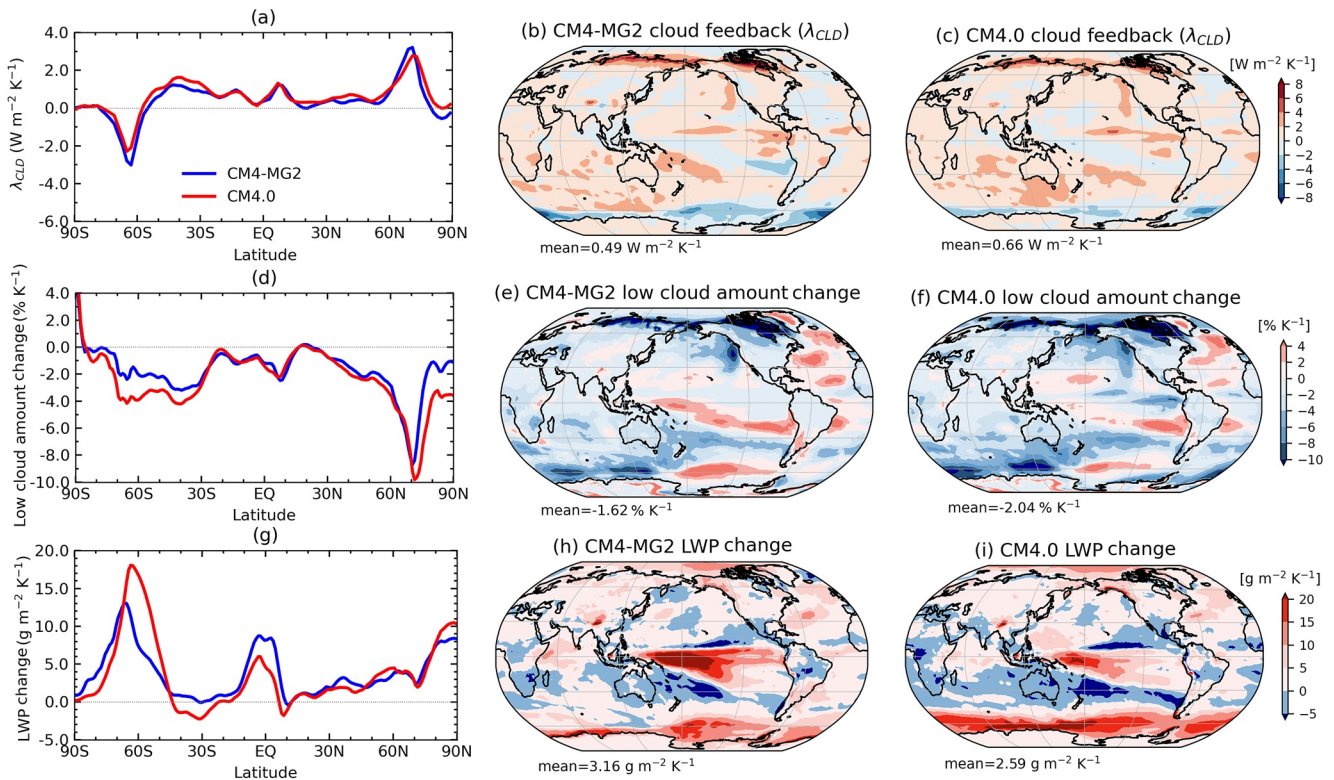


Figure 17. Zonal mean cloud feedback parameter (λ_{CLD}) in (a), low cloud amount feedback in (d), and liquid water path (LWP) feedback in (g), and their geographical distributions from CM4-MG2 in (b, e, and h), and from CM4.0 in (c, f, and i). λ_{CLD} is estimated using the radiative kernels based on the Geophysical Fluid Dynamics Laboratory model (Soden et al., 2008). The low cloud amount feedback is calculated by linearly regressing the percentage change in low cloud amount against surface air temperature change (ΔT). The LWP feedback is calculated by linearly regressing the change in LWP against ΔT .

be due to aerosol effects, climate sensitivity, and other factors. Given that climate sensitivity in CMIP6 GCMs increases substantially compared to that in CMIP5 models and that high sensitivity likely degrades the quality of the 20th century simulation and future projection, further research on climate sensitivity or cloud feedback is a high priority. Meanwhile, a credible 20th century simulation under the temperature trend constraint does not necessarily satisfy the “bottom-up” process level constraint such as cloud droplet size and cloud water phase partition (Bodas-Salcedo et al., 2019; Golaz et al., 2013; Suzuki et al., 2013). Future model development also needs to take the observational constraints on process level into account, in addition to the “top-down” constraints such as TOA radiative fluxes, atmospheric state, and temperature trend (Held et al., 2019; Mülmenstädt et al., 2020).

Appendix A: Model Tunings in CM4-MG2

We list parameter changes from CM4.0 to CM4-MG2 in Table A1.

Table A1
Model Parameters Modified in the CM4-MG2 Tuning Compared to CM4.0

Tuning parameter	Description	Configuration	
		CM4-MG2	CM4.0
vfact (dimensionless)	scaling factor for ice fall velocity	0.91	0.90
accretion_scale (dimensionless)	scaling factor for accretion rate	1.3	1.0
var_limit (m s ⁻¹)	minimum standard deviation of sub-grid vertical velocity	0.3	0.7
eros_scale_c (×10 ⁻⁶ s ⁻¹)	erosion constant under convective conditions	4.7	40
rkm_dp1 (km ⁻¹)	lateral mixing rate in deep convective plume	1.1	0.9
peff_i_d (×10 ⁻⁵ Pa ⁻¹)	convective precipitation efficiency	13	11

Data Availability Statement

The CM4.0 source codes are available at <https://doi.org/10.5281/zenodo.3339397>. The CM4.0 model data have been deposited in the CMIP6 archive with the identifier <https://doi.org/10.22033/ESGF/CMIP6.1402> and <https://doi.org/10.22033/ESGF/CMIP6.8594>. The original MG2 source code was from the CESM2.1.3 release, which can be downloaded at http://www.cesm.ucar.edu/models/cesm2/release_download.html. The CM4-MG2 source codes can be found at <https://doi.org/10.5281/zenodo.6323646>. The CM4-MG2 model data is available at <ftp://data1.gfdl.noaa.gov/users/huan.guo/microphysics/CM4-MG2>. The radiative kernels for calculating the cloud feedback are accessible via <https://climate.rsmas.miami.edu/data/radiative-kernels/index.html>. The CERES-EBAF and GPCP data can be obtained from <https://ceres.larc.nasa.gov/data> and <https://psl.noaa.gov/data/gridded/data.gpcp.html>, respectively. The GISS Surface Temperature Analysis (GISTEMP v4) is accessible via <https://data.giss.nasa.gov/gistemp>. The HadISST data set can be downloaded at <https://www.metoffice.gov.uk/hadobs/hadisst/data/download.html>. The NOAA Extended Reconstructed Sea Surface Temperature (SST) V5 is available at <https://psl.noaa.gov/data/gridded/data.noaa.ersst.v5.html>. Data from the RAPID AMOC monitoring project are freely available from www.rapid.ac.uk/rapidmoc (<https://doi.org/10.5285/aa57e879-4cca-28b6-e053-6c86abc02de5>). The ERA-Interim (European Center for Medium Range Weather Forecasting Re-Analysis Interim) and ERA5 data are available at <https://www.ecmwf.int/en/research/climate-reanalysis/era-interim> and <https://www.ecmwf.int/en/forecasts/datasets/reanalysis-datasets/era5>, respectively.

Acknowledgments

Dr. Mitchell Bushuk and Dr. David Paynter are acknowledged for their comments and suggestions on an internal review of the manuscript. We thank three anonymous reviewers for providing insightful comments that led to improvement of the manuscript. L. Zhou is supported under awards NA18OAR4320123, NA19OAR0220146, and NA19OAR0220147 from the National Oceanic and Atmospheric Administration (NOAA), U.S. Department of Commerce.

References

- Adames, Á. F., & Wallace, J. M. (2015). Three-dimensional structure and evolution of the moisture field in the MJO. *Journal of the Atmospheric Sciences*, 72(10), 3733–3754. <https://doi.org/10.1175/JAS-D-15-0003.1>
- Aderoft, A., Anderson, W., Balaji, V., Blanton, C., Bishuk, M., Dufour, C. O., et al. (2019). The GFDL global ocean and sea ice model OM4.0: Model description and simulation features. *Journal of Advances in Modeling Earth Systems*, 11(10), 3167–3211. <https://doi.org/10.1029/2019MS001726>
- Aderoft, A., & Hallberg, R. (2006). On methods for solving the oceanic equations of motion in generalized vertical coordinates. *Ocean Modelling*, 11(1), 224–233. <https://doi.org/10.1016/j.ocemod.2004.12.007>
- Adler, R. F., Huffman, G. J., Chang, A., Ferraro, R., Xie, P., Janowiak, J., et al. (2003). The version 2 global precipitation climatology project (GPCP) monthly precipitation analysis (1979–present). *Journal of Hydrometeorology*, 4(6), 1147–1167. [https://doi.org/10.1175/1525-7541\(2003\)004<1147:tvGPCP>2.0.CO;2](https://doi.org/10.1175/1525-7541(2003)004<1147:tvGPCP>2.0.CO;2)
- Adler, R. F., Sapiano, M., Huffman, G., Bolvin, D., Gu, G., Wang, J., et al. (2016). *The new version 2.3 of the global precipitation climatology project (GPCP) monthly analysis product (internal report)*. Earth System Science Interdisciplinary Center, University of Maryland.
- Alexander, M. J., & Dunkerton, T. J. (1999). A spectral parameterization of mean-flow forcing due to breaking gravity waves. *Journal of the Atmospheric Sciences*, 56(24), 4167–4182. [https://doi.org/10.1175/1520-0469\(1999\)056<4167:ASPOMF>2.0.CO;2](https://doi.org/10.1175/1520-0469(1999)056<4167:ASPOMF>2.0.CO;2)
- Andrews, T., Andrews, M. B., Bodas-Salcedo, A., Jones, G. S., Kuhlbrodt, T., Manners, J., et al. (2019). Forcing, feedbacks and climate sensitivity in HadGEM3-GC3.1 and UKESM1. *Journal of Advances in Modeling Earth Systems*, 11(12), 4377–4394. <https://doi.org/10.1029/2019MS001866>
- Andrews, T., Gregory, J. M., Webb, M. J., & Taylor, K. E. (2012). Forcing, feedbacks and climate sensitivity in CMIP5 coupled atmosphere-ocean climate models. *Geophysical Research Letters*, 39(9), L09712. <https://doi.org/10.1029/2012GL051607>
- Antonov, J. I., Locarnini, R. A., Boyer, T. P., Mishonov, A. V., & Garcia, H. E. (2006). World Ocean Atlas 2005, volume 2: Salinity. In S. Levitus (Ed.), *NOAA Atlas NESDIS 62* (pp. 1–182). U.S. Government Printing Office.
- Balaji, V. (2012). The flexible modeling system. In *Earth system modelling-volume 3* (pp. 33–41). Springer.
- Benedict, J. J., Maloney, E. D., Sobel, A. H., & Frierson, D. M. W. (2014). Gross moist stability and MJO simulation skill in three full-physics GCMs. *Journal of the Atmospheric Sciences*, 71(9), 3327–3349. <https://doi.org/10.1175/JAS-D-13-0240.1>
- Bleck, R. (2002). An oceanic general circulation model framed in hybrid isopycnic-Cartesian coordinates. *Ocean Modelling*, 4(1), 55–88. [https://doi.org/10.1016/S1463-5003\(01\)00012-9](https://doi.org/10.1016/S1463-5003(01)00012-9)

- Bodas-Salcedo, A., Mulcahy, J. P., Andrews, T., Williams, K. D., Ringer, M. A., Field, P. R., & Elsaesser, G. S. (2019). Strong dependence of atmospheric feedbacks on mixed-phase microphysics and aerosol-cloud interactions in HadGEM3. *Journal of Advances in Modeling Earth Systems*, 11(6), 1735–1758. <https://doi.org/10.1029/2019MS001688>
- Bogenschutz, P. A., Yamaguchi, T., & Lee, H.-H. (2021). The energy exascale earth system model simulations with high vertical resolution in the lower troposphere. *Journal of Advances in Modeling Earth Systems*, 13(6), e2020MS002239. <https://doi.org/10.1029/2020MS002239>
- Brient, F., Schneider, T., Tan, Z., Bony, S., Qu, X., & Hall, A. (2015). Shallowness of tropical low clouds as a predictor of climate models' response to warming. *Climate Dynamics*, 47(1–2), 433–449. <https://doi.org/10.1007/s00382-015-2846-0>
- Cavalieri, D. J., Parkinson, C. L., Gloersen, P., & Zwally, H. J. (1996). *Sea ice concentrations from Nimbus-7 SMMR and DMSP SSM/I-SSMIS passive microwave data, version 1*. NASA DAAC at the National Snow and Ice Data Center. <https://doi.org/10.5067/8GQ8LZQVLOVL>
- Cess, R. D., Potter, G. L., Blanchet, J. P., Boer, G. J., Del Genio, A. D., Deque, M., et al. (1990). Intercomparison and interpretation of climate feedback processes in 19 atmospheric general circulation models. *Journal of Geophysical Research*, 95(D10), 16601–16615. <https://doi.org/10.1029/jd095id10p16601>
- Danabasoglu, G., Lamarque, J., Bacmeister, J., Bailey, D. A., DuVivier, A. K., Edwards, J., et al. (2020). The community earth system model version 2 (CESM2). *Journal of Advances in Modeling Earth Systems*, 12(2). <https://doi.org/10.1029/2019MS001916>
- Dee, D. P., Uppala, S. M., Simmons, A. J., Berrisford, P., Poli, P., Kobayashi, S., et al. (2011). The ERA-Interim reanalysis: Configuration and performance of the data assimilation system. *Quarterly Journal of the Royal Meteorological Society*, 137(656), 553–597. <https://doi.org/10.1002/qj.828>
- Delworth, T. L., Broccoli, A. J., Rosati, A., Stouffer, R. J., Balaji, V., Beesley, J. A., et al. (2006). GFDL's CM2 global coupled climate models. Part I: Formulation and simulation characteristics. *Journal of Climate*, 19(5), 643–674. <https://doi.org/10.1175/JCLI3629.1>
- Delworth, T. L., Cooke, W. F., Adcroft, A., Bushuk, M., Chen, J. H., Dunne, K. A., et al. (2020). Spear: The next generation GFDL modeling system for seasonal to multidecadal prediction and projection. *Journal of Advances in Modeling Earth Systems*, 12(3), e2019MS001895. <https://doi.org/10.1029/2019MS001895>
- Delworth, T. L., & Dixon, K. W. (2006). Have anthropogenic aerosols delayed a greenhouse gas-induced weakening of the North Atlantic thermohaline circulation? *Geophysical Research Letters*, 33(2), L02606. <https://doi.org/10.1029/2005gl024980>
- Donner, L. J., Wyman, B. L., Hemler, R. S., Horowitz, L. W., Ming, Y., Zhao, M., et al. (2011). The dynamical core, physical parameterizations, and basic simulation characteristics of the atmospheric component AM3 of the GFDL global coupled model CM3. *Journal of Climate*, 24(13), 3484–3519. <https://doi.org/10.1175/2011jcli3955.1>
- Dunne, J. P., Horowitz, L. W., Adcroft, A. J., Ginoux, P., Held, I. M., John, J. G., et al. (2020). The GFDL Earth System Model Version 4.1 (GFDL-ESM 4.1): Overall coupled model description and simulation characteristics. *Journal of Advances in Modeling Earth Systems*, 12(11), e2019MS002015. <https://doi.org/10.1029/2019MS002015>
- Dunne, J. P., Winton, M., Bacmeister, J., Danabasoglu, G., Gettelman, A., Golaz, J., et al. (2020). Comparison of equilibrium climate sensitivity estimates from Slab Ocean, 150-year, and longer simulations. *Geophysical Research Letters*, 47(16), e2020GL088852. <https://doi.org/10.1029/2020GL088852>
- Elsaesser, G. S., O'Dell, C. W., Lebsock, D. M., Bennartz, R., Greenwald, T. J., & Wentz, F. J. (2017). The multi-sensor advanced climatology of liquid water path (MAC-LWP). *Journal of Climate*, 30(24), 10193–10210. <https://doi.org/10.1175/JCLI-D-16-0902.1>
- Eyring, V., Bony, S., Meehl, G. A., Senior, C. A., Stevens, B., Stouffer, R. J., & Taylor, K. E. (2016). Overview of the coupled model intercomparison project phase 6 (CMIP6) experimental design and organization. *Geoscientific Model Development*, 9(5), 1937–1958. <https://doi.org/10.5194/gmd-9-1937-2016>
- Fan, S., Ginoux, P., Seman, C. J., Silvers, L. G., & Zhao, M. (2019). Toward improved cloud-phase simulation with a mineral dust and temperature-dependent parameterization for ice nucleation in mixed-phase clouds. *Journal of the Atmospheric Sciences*, 76(11), 3655–3667. <https://doi.org/10.1175/JAS-D-18-0287.1>
- Fels, S., & Schwarzkopf, D. M. (1975). The simplified exchange approximation: A new method for radiative transfer calculations. *Journal of the Atmospheric Sciences*, 32(7), 1475–1488. [https://doi.org/10.1175/1520-0469\(1975\)032<1475:tsean>2.0.co;2](https://doi.org/10.1175/1520-0469(1975)032<1475:tsean>2.0.co;2)
- Forster, P. M., Richardson, T., Maycock, A. C., Smith, C. J., Samsel, B. H., Myhre, G., et al. (2016). Recommendations for diagnosing effective radiative forcing from climate models for CMIP6. *Journal of Geophysical Research: Atmospheres*, 121(20), 12460–12475. <https://doi.org/10.1002/2016JD025320>
- Freidenreich, S. M., & Ramaswamy, V. (2005). Refinement of the geophysical fluid dynamics laboratory solar benchmark computations and an improved parameterization for climate models. *Journal of Geophysical Research*, 110(D17), D17105. <https://doi.org/10.1029/2004JD005471>
- Fu, Q., Krueger, S. K., & Liou, K. N. (1995). Interactions between radiation and convection in simulated tropical cloud clusters. *Journal of the Atmospheric Sciences*, 52(9), 1310–1328. [https://doi.org/10.1175/1520-0469\(1995\)052<1310:ioraci>2.0.co;2](https://doi.org/10.1175/1520-0469(1995)052<1310:ioraci>2.0.co;2)
- Garner, S. T. (2005). A topographic drag closure built on an analytical base flux. *Journal of the Atmospheric Sciences*, 62(7), 2302–2315. <https://doi.org/10.1175/jas3496.1>
- Garner, S. T. (2018). Ground-truth model evaluation of subgrid orographic base-flux parameterization. *Journal of the Atmospheric Sciences*, 75(10), 3653–3670. <https://doi.org/10.1175/jas-d-17-0368.1>
- Gent, P. R., Yeager, S. G., Neale, R. B., Levis, S., & Bailey, D. A. (2010). Improvements in a half degree atmosphere/land version of the CCSM. *Climate Dynamics*, 34(6), 819–833. <https://doi.org/10.1007/s00382-009-0614-8>
- Gettelman, A., Morrison, H., Santos, S., Bogenschutz, P., & Caldwell, P. M. (2015a). Advanced two-moment bulk microphysics for global models. Part I: Off-line tests and comparison with other schemes. *Journal of Climate*, 28(3), 1268–1287. <https://doi.org/10.1175/JCLI-D-14-00103.1>
- Gettelman, A., Morrison, H., Santos, S., Bogenschutz, P., & Caldwell, P. M. (2015b). Advanced two-moment bulk microphysics for global models. Part II: Global model solutions and aerosol-cloud interactions. *Journal of Climate*, 28(3), 1288–1306. <https://doi.org/10.1175/JCLI-D-14-00102.1>
- Gettelman, A., Morrison, H., Terai, C. R., & Wood, R. (2013). Microphysical process rates and global aerosol–cloud interactions. *Atmospheric Chemistry and Physics*, 13(11), 11789–11825. <https://doi.org/10.5194/acpd-13-11789-2013>
- GFDL Global Atmosphere Model Development Team. (2004). The new GFDL global atmosphere and land model AM2-LM2: Evaluation with prescribed SST simulations. *Journal of Climate*, 17, 4641–4673. <https://doi.org/10.1175/JCLI-3223.1>
- Ghan, S. J., Leung, L. R., Easter, R. C., & Abdul-Razzak, H. (1997). Prediction of cloud droplet number in a general circulation model. *Journal of Geophysical Research*, 102(D18), 21777–21794. <https://doi.org/10.1029/97JD01810>
- GISTEMP-Team. (2019). GISS surface temperature analysis (GISTEMP), version 4 [Dataset]. NASA Goddard Institute for Space Studies, Retrieved from <https://data.giss.nasa.gov/gistemp/>
- Golaz, J.-C., Caldwell, P. M., Van Roekel, L. P., Petersen, M. R., Tang, Q., Wolfe, J. D., et al. (2019). The DOE E3SM coupled model version 1: Overview and evaluation at standard resolution. *Journal of Advances in Modeling Earth Systems*, 11(7), 2089–2129. <https://doi.org/10.1029/2018MS001603>

- Golaz, J.-C., Horowitz, L. W., & Levy, H. (2013). Cloud tuning in a coupled climate model: Impact on 20th century warming. *Geophysical Research Letters*, *40*(10), 2246–2251. <https://doi.org/10.1002/grl.50232>
- Golaz, J.-C., Salzmann, M., Donner, L. J., Horowitz, L. W., Ming, Y., & Zhao, M. (2011). Sensitivity of the aerosol indirect effect to subgrid variability in the cloud parameterization of the GFDL atmosphere general circulation model AM3. *Journal of Climate*, *24*(13), 3145–3160. <https://doi.org/10.1175/2010JCLI3945.1>
- Gregory, J., Ingram, W., Palmer, M., Jones, G., Stott, P., Thorpe, R., & Williams, K. (2004). A new method for diagnosing radiative forcing and climate sensitivity. *Geophysical Research Letters*, *31*(3), L03205. <https://doi.org/10.1029/2003gl018747>
- Gregory, J. M., & Forster, P. M. (2008). Transient climate response estimated from radiative forcing and observed temperature change. *Journal of Geophysical Research*, *113*(D23), D23105. <https://doi.org/10.1029/2008JD010405>
- Guilyardi, E., Capotondi, A., Lengaigne, M., Thual, S., & Wittenberg, A. T. (2020). ENSO modeling: History, progress, and challenges. In M. J. McPhaden, A. Santoso, & W. Cai (Eds.), (pp. 201–226). American Geophysical Union. <https://doi.org/10.1002/9781119548164.ch9>
- Guo, H., Ming, Y., Fan, S., Zhou, L., Harris, L., & Zhao, M. (2021). Two-moment bulk cloud microphysics with prognostic precipitation in GFDL's atmosphere model AM4.0: Configuration and performance. *Journal of Advances in Modeling Earth Systems*, *13*(6), e2020MS002453. <https://doi.org/10.1029/2020MS002453>
- Hansen, J., Sato, M., Ruedy, R., Nazarenko, L., Lacis, A., Schmidt, G. A., et al. (2014). Efficacy of climate forcings. *Journal of Geophysical Research: Atmospheres*, *119*(D18), D18104. <https://doi.org/10.1029/2005jd005776>
- Harris, I., Jones, P., Osborn, T., & Lister, D. (2014). Updated high-resolution grids of monthly climatic observations—The CRU TS3.10 dataset. *International Journal of Climatology*, *34*(3), 623–642. <https://doi.org/10.1002/joc.3711>
- Harris, L., Zhou, L., Chen, X., & Chen, J.-H. (2020). The GFDL finite-volume cubed-sphere dynamical core. In NOAA technical memorandum. OAR GFDL. <https://doi.org/10.25923/h88-c534>
- Hassan, T., Allen, R. J., Liu, W., & Randles, C. A. (2021). Anthropogenic aerosol forcing of the Atlantic meridional overturning circulation and the associated mechanisms in CMIP6 models. *Atmospheric Chemistry and Physics*, *21*(8), 5821–5846. <https://doi.org/10.5194/acp-21-5821-2021>
- Held, I. M., Guo, H., Adcroft, A., Dunne, J. P., Horowitz, L. W., Krasting, J., et al. (2019). Structure and performance of GFDL's CM4.0 climate model. *Journal of Advances in Modeling Earth Systems*, *11*(11), 3691–3727. <https://doi.org/10.1029/2019MS001829>
- Huang, B., Thorne, P. W., Banzon, V. F., Boyer, T., Chepurin, G., Lawrimore, J. H., et al. (2017). Extended reconstructed sea surface temperature, version 5 (ERSSTv5): Upgrades, validations, and intercomparisons. *Journal of Climate*, *30*(20), 8179–8205. <https://doi.org/10.1175/JCLI-D-16-0836.1>
- IPCC. (2021). Climate change 2021: The physical science basis. In V. Masson-Delmotte, P. Zhai, A. Pirani, Sarah L. Connors, C. Péan, Y. Chen, et al. (Eds.). In *Contribution of working group I to the sixth assessment report of the intergovernmental panel on climate change*. Cambridge University Press. <https://doi.org/10.1017/9781009157896>
- Jakob, C., & Klein, S. A. G. (2000). A parameterization of the effects of cloud and precipitation overlap for use in general circulation models. *The Quarterly Journal of the Royal Meteorological Society*, *126*(568), 2525–2544. <https://doi.org/10.1002/qj.49712656809>
- Jiang, J., Su, H., Zhai, C., Perun, V., Del Genio, A., Nazarenko, L. S., et al. (2012). Evaluation of cloud and water vapor simulations in CMIP5 climate models using NASA A-train satellite observations. *Journal of Geophysical Research*, *117*(D14). <https://doi.org/10.1029/2011JD017237>
- Jiang, X. (2017). Key processes for the eastward propagation of the Madden-Julian Oscillation based on multimodel simulations. *Journal of Geophysical Research: Atmospheres*, *122*(2), 755–770. <https://doi.org/10.1002/2016JD025955>
- Jiang, X., Adames, Á. F., Kim, D., Maloney, E. D., Lin, H., Kim, H., et al. (2020). Fifty years of research on the Madden-Julian Oscillation: Recent progress, challenges, and perspectives. *Journal of Geophysical Research: Atmospheres*, *125*(17), e2019JD030911. <https://doi.org/10.1029/2019JD030911>
- Kelley, M., Schmidt, G. A., Nazarenko, L., Bauer, S. E., Ruedy, R., Russell, G. L., et al. (2020). GISS-E2.1: Configurations and climatology. *Journal of Advances in Modeling Earth Systems*, *12*(8). <https://doi.org/10.1029/2019MS002025>
- Kessler, E., Feteris, P. J., & Newburg, E. A. (1963). Role of microphysical processes in shaping vertical profiles of precipitation and cloud. In *Proceedings tenth weather radar conference* (pp. 91–97).
- Kessler, W. S. (2002). Is ENSO a cycle or a series of events? *Geophysical Research Letters*, *29*(23), 401–404. <https://doi.org/10.1029/2002GL015924>
- Kim, H.-M. (2017). The impact of the mean moisture bias on the key physics of MJO propagation in the ECMWF reforecast. *Journal of Geophysical Research: Atmospheres*, *122*(15), 7772–7784. <https://doi.org/10.1002/2017JD027005>
- Kim, W. M., Yeager, S., Chang, P., & Danabasoglu, G. (2017). Low-frequency North Atlantic climate variability in the community earth system model large ensemble. *Journal of Climate*, *31*(2), 787–813. <https://doi.org/10.1175/JCLI-D-17-0193.1>
- Kristjansson, J. E., Edwards, J. M., & Mitchell, D. L. (2000). Impact of a new scheme for optical properties of ice crystals on climates of two GCMS. *Journal of Geophysical Research*, *105*(D8), 10063–10079. <https://doi.org/10.1029/2000jd900015>
- Kuhlbrot, T., Jones, C. G., Sellar, A., Storkey, D., Blockley, E., Stringer, M., et al. (2018). The low-resolution version of HadGEM3 GC3.1: Development and evaluation for global climate. *Journal of Advances in Modeling Earth Systems*, *10*(11), 2865–2888. <https://doi.org/10.1029/2018MS001370>
- Larkin, N. K., & Harrison, D. E. (2002). ENSO warm (El Niño) and cold (La Niña) event life cycles: Ocean surface anomaly patterns, their symmetries, asymmetries, and implications. *Journal of Climate*, *15*(10), 1118–1140. [https://doi.org/10.1175/1520-0442\(2002\)015<1118:EWENOA>2.0.CO;2](https://doi.org/10.1175/1520-0442(2002)015<1118:EWENOA>2.0.CO;2)
- Lebsock, M., Morrison, H., & Gettelman, A. (2013). Microphysical implications of cloud-precipitation covariance derived from satellite remote sensing. *Journal of Geophysical Research: Atmospheres*, *118*(12), 6521–6533. <https://doi.org/10.1002/jgrd.50347>
- Lee, H.-H., Bogenschütz, P., & Yamaguchi, T. (2021). The implementation of framework for improvement by vertical enhancement into Energy Exascale Earth System Model. *Journal of Advances in Modeling Earth Systems*, *13*(6), e2020MS002240. <https://doi.org/10.1029/2020MS002240>
- Lenssen, N., Schmidt, G., Hansen, J., Menne, M., Persin, A., Ruedy, R., & Zyss, D. (2019). Improvements in the GISTEMP uncertainty model. *Journal of Geophysical Research: Atmospheres*, *124*(12), 6307–6326. <https://doi.org/10.1029/2018JD029522>
- Liebmann, B., & Smith, C. A. (1996). Description of a complete (interpolated) outgoing longwave radiation dataset. *Bulletin of the American Meteorological Society*, *77*, 1275–1277.
- Lin, S.-J. (2004). A “vertically Lagrangian” finite-volume dynamical core for global models. *Monthly Weather Review*, *132*(10), 2293–2307. [https://doi.org/10.1175/1520-0493\(2004\)132<2293:AVLFDC>2.0.CO;2](https://doi.org/10.1175/1520-0493(2004)132<2293:AVLFDC>2.0.CO;2)
- Locarnini, R. A., Mishonov, A. V., Antonov, J. I., Boyer, T. P., & Garcia, H. E. (2006). World Ocean Atlas 2005, volume 1: Temperature. In S. Levitus (Ed.), *NOAA Atlas NESDIS 61* (pp. 1–182). U.S. Government Printing Office.
- Lock, A. P., Brown, A. R., Bush, M. R., Martin, G. M., & Smith, R. N. B. (2000). A new boundary layer mixing scheme. Part I: Scheme description and single-column model tests. *Monthly Weather Review*, *128*(9), 3187–3199. [https://doi.org/10.1175/1520-0493\(2000\)128<3187:anblms>2.0.co;2](https://doi.org/10.1175/1520-0493(2000)128<3187:anblms>2.0.co;2)

- Loeb, N. G., Doelling, D. R., Wang, H., Su, W., Nguyen, C., Corbett, J. G., et al. (2018). Clouds and the Earth's radiant energy system (CERES) energy balanced and filled (EBAF) top-of-atmosphere (TOA) edition-4.0 data product. *Journal of Climate*, *31*(2), 895–918. <https://doi.org/10.1175/jcli-d-17-0208.1>
- Loeb, N. G., Wielicki, B. A., Doelling, D. R., Smith, G. L., Keyes, D. F., Kato, S., et al. (2009). Toward optimal closure of the Earth's top-of-atmosphere radiation budget. *Journal of Climate*, *22*(3), 748–766. <https://doi.org/10.1175/2008jcli2637.1>
- Lohmann, U., Rotstajn, L., Storelvmo, T., Jones, A., Menon, S., Quaas, J., et al. (2010). Total aerosol effect: Radiative forcing or radiative flux perturbation? *Atmospheric Chemistry and Physics*, *10*(7), 3235–3246. <https://doi.org/10.5194/acp-10-3235-2010>
- Madden, R. A., & Julian, P. R. (1971). Detection of a 40–50 day oscillation in the zonal wind in the tropical Pacific. *Journal of the Atmospheric Sciences*, *28*(5), 702–708. [https://doi.org/10.1175/1520-0469\(1971\)028<0702:doadoi>2.0.co;2](https://doi.org/10.1175/1520-0469(1971)028<0702:doadoi>2.0.co;2)
- Madden, R. A., & Julian, P. R. (1972). Description of global-scale circulation cells in the tropics with a 40–50 day period. *Journal of the Atmospheric Sciences*, *29*(6), 1109–1123. [https://doi.org/10.1175/1520-0469\(1972\)029<1109:dogsc>2.0.co;2](https://doi.org/10.1175/1520-0469(1972)029<1109:dogsc>2.0.co;2)
- Manabe, S., & Bryan, K. (1969). Climate calculations with a combined ocean-atmosphere model. *Journal of the Atmospheric Sciences*, *26*(4), 786–789. [https://doi.org/10.1175/1520-0469\(1969\)026\(0786:CCWACO\)2.0.CO;2](https://doi.org/10.1175/1520-0469(1969)026(0786:CCWACO)2.0.CO;2)
- Manabe, S., Bryan, K., & Spelman, M. (1975). A global ocean-atmosphere climate model. Part I. The atmospheric circulation. *Journal of Physical Oceanography*, *5*(1), 3–29. [https://doi.org/10.1175/1520-0485\(1975\)005<0003:agoacm>2.0.co;2](https://doi.org/10.1175/1520-0485(1975)005<0003:agoacm>2.0.co;2)
- Manabe, S., & Stouffer, R. J. (1988). Two stable equilibria of a coupled ocean-atmosphere model. *Journal of Climate*, *1*(9), 841–866. [https://doi.org/10.1175/1520-0442\(1988\)001<0841:tseac>2.0.co;2](https://doi.org/10.1175/1520-0442(1988)001<0841:tseac>2.0.co;2)
- M. J. McPhaden, A. Santoso, & W. Cai (Eds.) (2020). *El Niño Southern Oscillation in a Changing Climate*. American Geophysical Union. <https://doi.org/10.1002/9781119548164>
- Menary, M. B., Robson, J., Allan, R. P., Booth, B. B., Cassou, C., Gastineau, G., et al. (2020). Aerosol-forced AMOC changes in CMIP6 historical simulations. *Geophysical Research Letters*, *47*(14). <https://doi.org/10.1029/2020GL088166>
- Meyers, M. P., DeMott, P. J., & Cotton, W. R. (1992). New primary ice nucleation parameterizations in an explicit cloud model. *Journal of Applied Meteorology*, *32*(7), 708–721. [https://doi.org/10.1175/1520-0450\(1992\)031<0708:npinpi>2.0.co;2](https://doi.org/10.1175/1520-0450(1992)031<0708:npinpi>2.0.co;2)
- Milly, P. C., Malyshev, S. L., Shevliakova, E., Dunne, K. A., Findell, K. L., Gleeson, T., et al. (2014). An enhanced model of land water and energy for global hydrologic and earth-system studies. *Journal of Hydrometeorology*, *15*(5), 1739–1761. <https://doi.org/10.1175/jhm-d-13-01162.1>
- Ming, Y., Ramaswamy, V., Donner, L. J., & Phillips, V. T. J. (2006). A new parameterization of cloud droplet activation applicable to General Circulation Models. *Journal of the Atmospheric Sciences*, *63*(4), 1348–1356. <https://doi.org/10.1175/jas3686.1>
- Ming, Y., Ramaswamy, V., Donner, L. J., Phillips, V. T. J., Klein, S. A., Ginoux, P. A., & Horowitz, L. W. (2007). Modeling the interactions between aerosols and liquid water clouds with a self-consistent cloud scheme in a General Circulation Model. *Journal of the Atmospheric Sciences*, *64*(4), 1189–1209. <https://doi.org/10.1175/JAS3874.1>
- Moat, B. I., Frajka-Williams, E., Smeed, D., Rayner, D., Sanchez-Franks, A., Johns, W. E., et al. (2020). Atlantic meridional overturning circulation observed by the RAPID-MOCHA-WBTS (RAPID-Meridional overturning circulation and heatflux array-western boundary time series) array at 26N from 2004 to 2018. (v2018.2). <https://doi.org/10.5285/57e879-4cca-28b6-e053-6c86abc02de5>
- Morrison, H., & Gettelman, A. (2008). A new two-moment bulk stratiform cloud microphysics scheme in the Community Atmosphere Model, version 3 (CAM3). Part I: Description and numerical tests. *Journal of Climate*, *21*(15), 3642–3659. <https://doi.org/10.1175/2008JCLI2105.1>
- Mülmenstädt, J., Nam, C., Salzmann, M., Kretschmar, J., L'Ecuyer, T. S., Lohmann, U., et al. (2020). Reducing the aerosol forcing uncertainty using observational constraints on warm rain processes. *Science Advances*, *6*(22), eaaz6433. <https://doi.org/10.1126/sciadv.aaz6433>
- Paynter, D. J., & Ramaswamy, V. (2012). Variations in water vapor continuum radiative transfer with atmospheric conditions. *Journal of Geophysical Research*, *117*, D16310. <https://doi.org/10.1029/2012JD017504>
- Paynter, D. J., & Ramaswamy, V. (2014). Investigating the impact of the shortwave water vapor continuum upon climate simulations using GFDL global models. *Journal of Geophysical Research: Atmospheres*, *119*(18), 10720–10737. <https://doi.org/10.1002/2014JD021881>
- Posselt, R., & Lohmann, U. (2008). Introduction of prognostic rain in ECHAM5: Design and single column model simulations. *Atmospheric Chemistry and Physics*, *8*(11), 2949–2963. <https://doi.org/10.5194/acp-8-2949-2008>
- Posselt, R., & Lohmann, U. (2009). Sensitivity of the total anthropogenic aerosol effect to the treatment of rain in a global climate model. *Geophysical Research Letters*, *36*(2), L02805. <https://doi.org/10.1029/2008GL035796>
- Pritchard, M. S., & Bretherton, C. S. (2014). Causal evidence that rotational moisture advection is critical to the superparameterized Madden-Julian Oscillation. *Journal of the Atmospheric Sciences*, *71*(2), 800–815. <https://doi.org/10.1175/JAS-D-13-01119.1>
- Putman, W. M., & Lin, S.-J. (2007). Finite-volume transport on various cubed-sphere grids. *Journal of Computational Physics*, *227*(1), 55–78. <https://doi.org/10.1016/j.jcp.2007.07.022>
- Quaas, J., Ming, Y., Menon, S., Takemura, T., Wang, M., Penner, J. E., et al. (2009). Aerosol indirect effects—General circulation model intercomparison and evaluation with satellite data. *Atmospheric Chemistry and Physics*, *9*(22), 8697–8717. <https://doi.org/10.5194/acp-9-8697-2009>
- Rayner, N., Parker, D. E., Horton, E., Folland, C. K., Alexander, L. V., Rowell, D., & Kaplan, A. (2003). Global analyses of sea surface temperature, sea ice, and night marine air temperature since the late nineteenth century. *Journal of Geophysical Research*, *108*(D14), 4407. <https://doi.org/10.1029/2002jd002670>
- Ringer, M., Andrews, T., & Webb, M. (2014). Global-mean radiative feedbacks and forcing in atmosphere-only and coupled atmosphere–ocean climate change experiments. *Geophysical Research Letters*, *41*(11), 4035–4042. <https://doi.org/10.1002/2014gl060347>
- Ringer, M., McAvaney, B. J., Andronova, N., Buja, L. E., Esch, M., Ingram, W. J., et al. (2006). Global mean cloud feedbacks in idealized climate change experiments. *Geophysical Research Letters*, *33*(7), L07718. <https://doi.org/10.1029/2005gl025370>
- Rosenblum, E., Fajber, R., Stroeve, J. C., Gille, S. T., Tremblay, L. B., & Carmack, E. C. (2021). Surface salinity under transitioning ice cover in the Canada basin: Climate model biases linked to vertical distribution of fresh water. *Geophysical Research Letters*, *48*(21). <https://doi.org/10.1029/2021gl094739>
- Rotstajn, L., Ryan, B. F., & Katzfey, J. J. (2000). A scheme for calculation of the liquid fraction in mixed-phase stratiform clouds in large-scale models. *Monthly Weather Review*, *128*(4), 1070–1088. [https://doi.org/10.1175/1520-0493\(2000\)128<1070:ascfot>2.0.co;2](https://doi.org/10.1175/1520-0493(2000)128<1070:ascfot>2.0.co;2)
- Rotstajn, L. D. (1997). A physically based scheme for the treatment of stratiform clouds and precipitation in large-scale models. I, Description and evaluation of the microphysical processes. *Quarterly Journal of the Royal Meteorological Society*, *123*(541), 1227–1282. <https://doi.org/10.1256/smsqj.54105>
- Salzmann, M., Ming, Y., Golaz, J.-C., Ginoux, P. A., Morrison, H., Gettelman, A., et al. (2010). Two-moment bulk stratiform cloud microphysics in the GFDL AM3 GCM: Description, evaluation, and sensitivity tests. *Atmospheric Chemistry and Physics*, *10*(16), 8037–8064. <https://doi.org/10.5194/acp-10-8037-2010>
- Sato, Y., Goto, D., Michibata, T., Suzuki, K., Takemura, T., Tomita, H., & Nakajima, T. (2018). Aerosol effects on cloud water amounts were successfully simulated by a global cloud-system resolving model. *Nature Communications*, *9*(985), 985. <https://doi.org/10.1038/s41467-018-03379-6>
- Savijarvi, H. (1997). Shortwave optical properties of rain. *Tellus*, *49a*(2), 177–181. <https://doi.org/10.3402/tellusa.v49i2.14463>

- Schwarzkopf, D. M., & Fels, S. (1991). The simplified exchange method revisited: An accurate, rapid method for computation of infrared cooling rates and fluxes. *Journal of Geophysical Research*, *96*(D5), 9075–9096. <https://doi.org/10.1029/89jd01598>
- Seifert, A., & Beheng, K. D. (2001). A double-moment parameterization for simulating autoconversion, accretion and selfcollection. *Atmospheric Research*, *59–60*, 265–281. [https://doi.org/10.1016/s0169-8095\(01\)00126-0](https://doi.org/10.1016/s0169-8095(01)00126-0)
- Sherwood, S. C., Webb, M. J., Annan, J. D., Armour, K. C., Forster, P. M., Hargreaves, J. C., et al. (2020). An assessment of Earth's climate sensitivity using multiple lines of evidence. *Reviews of Geophysics*, *58*(4), e2019RG000678. <https://doi.org/10.1029/2019RG000678>
- Shevliakova, E., Pacala, S. W., Malyshev, S., Hurtt, G. C., Milly, P., Caspersen, J. P., et al. (2009). Carbon cycling under 300 years of land use change: Importance of the secondary vegetation sink. *Global Biogeochemical Cycles*, *23*(2). <https://doi.org/10.1029/2007gb003176>
- Soden, B. J., Broccoli, A., & Hemler, R. (2004). On the use of cloud forcing to estimate cloud feedback. *Journal of Climate*, *17*(19), 3661–3665. [https://doi.org/10.1175/1520-0442\(2004\)017<3661:OTUOCF>2.0.CO;2](https://doi.org/10.1175/1520-0442(2004)017<3661:OTUOCF>2.0.CO;2)
- Soden, B. J., Held, I. M., Colman, R., Shell, K. M., Kiehl, J. T., & Shields, C. A. (2008). Quantifying climate feedbacks using radiative kernels. *Journal of Climate*, *21*(14), 3504–3520. <https://doi.org/10.1175/2007JCLI2110.1>
- Storelvmo, T., Kristjánsson, J. E., Ghan, S. J., Kirkevåg, A., Seland, Ø., & Iversen, T. (2006). Predicting cloud droplet number concentration in Community Atmosphere Model (CAM)-Oslo. *Journal of Geophysical Research*, *11*(D24), D24208. <https://doi.org/10.1029/2005JD006300>
- Sui, C.-H., Li, X., & Yang, M.-J. (2007). On the definition of precipitation efficiency. *Journal of the Atmospheric Sciences*, *64*(12), 4506–4513. <https://doi.org/10.1175/2007JAS2332.1>
- Sui, C.-H., Li, X., Yang, M.-J., & Huang, H.-L. (2005). Estimation of oceanic precipitation efficiency in cloud models. *Journal of the Atmospheric Sciences*, *62*(12), 4358–4370. <https://doi.org/10.1175/JAS3587.1>
- Suzuki, K., Golaz, J. C., & Stephens, G. L. (2013). Evaluating cloud tuning in a climate model with satellite observations. *Geophysical Research Letters*, *40*(16), 4464–4468. <https://doi.org/10.1002/grl.50874>
- Tan, I., Storelvmo, T., & Zelinka, M. D. (2016). Observational constraints on mixed-phase clouds imply higher climate sensitivity. *Science*, *352*(6282), 224–227. <https://doi.org/10.1126/science.aad5300>
- Tiedtke, M. (1993). Representation of clouds in large-scale models. *Monthly Weather Review*, *121*(121), 3040–3061. [https://doi.org/10.1175/1520-0493\(1993\)121<3040:rocils>2.0.co;2](https://doi.org/10.1175/1520-0493(1993)121<3040:rocils>2.0.co;2)
- Toll, V., Christensen, M., Quaas, J., & Bellouin, N. (2019). Weak average liquid-cloud-water response to anthropogenic aerosols. *Nature*, *572*(7767), 51–55. <https://doi.org/10.1038/s41586-019-1423-9>
- Torrence, C., & Compo, G. P. (1998). A practical guide to wavelet analysis. *Bulletin of the American Meteorological Society*, *79*(1), 61–78. [https://doi.org/10.1175/1520-0477\(1998\)079<0061:apgtwa>2.0.co;2](https://doi.org/10.1175/1520-0477(1998)079<0061:apgtwa>2.0.co;2)
- Voldoire, A., Saint-Martin, D., Sénési, S., Decharme, B., Alias, A., Chevallier, M., et al. (2019). Evaluation of CMIP6 DECK experiments with CNRM-CM6-1. *Journal of Advances in Modeling Earth Systems*, *11*(7), 2177–2213. <https://doi.org/10.1029/2019MS001683>
- Vonder Haar, T. H., Bytheway, J. L., & Forsythe, J. M. (2012). Weather and climate analyses using improved global water vapor observations. *Geophysical Research Letters*, *39*(15), L16802. <https://doi.org/10.1029/2012GL052094>
- Wang, C., Soden, B. J., Yang, W., & Vecchi, G. A. (2021). Compensation between cloud feedback and aerosol-cloud interaction in CMIP6 models. *Geophysical Research Letters*, *48*(4), e2020GL091024. <https://doi.org/10.1029/2020GL091024>
- Wang, M., Ghan, S., Liu, X., L'Ecuyer, T. S., Zhang, K., Morrison, H., et al. (2012). Constraining cloud lifetime effects of aerosols using A-Train satellite observations. *Geophysical Research Letters*, *39*(15), L15709. <https://doi.org/10.1029/2012GL052204>
- Webb, M. J., Senior, C. A., Sexton, D. M. H., Ingram, W. J., Williams, K. D., Ringer, M. A., et al. (2006). On the contribution of local feedback mechanisms to the range of climate sensitivity in two GCM ensembles. *Climate Dynamics*, *27*(1), 17–38. <https://doi.org/10.1007/s00382-006-0111-2>
- Wheeler, M., & Kiladis, G. N. (1999). Convectively coupled equatorial waves: Analysis of clouds and temperature in the wavenumber-frequency domain. *Journal of the Atmospheric Sciences*, *56*(3), 374–399. [https://doi.org/10.1175/1520-0469\(1999\)056<0374:ccwao>2.0.co;2](https://doi.org/10.1175/1520-0469(1999)056<0374:ccwao>2.0.co;2)
- Winton, M., Adcroft, A., Dunne, J. P., Held, I. M., Shevliakova, E., Zhao, M., et al. (2020). Climate sensitivity of GFDL's CM4.0. *Journal of Advances in Modeling Earth Systems*, *12*(1), e2019MS001838. <https://doi.org/10.1029/2019MS001838>
- Wittenberg, A. T. (2009). Are historical records sufficient to constrain ENSO simulations? *Geophysical Research Letters*, *36*(12), L14709. <https://doi.org/10.1029/2009GL038710>
- Wittenberg, A. T., Rosati, A., Delworth, T. L., Vecchi, G. A., & Zeng, F. (2014). ENSO modulation: Is it decadal predictable? *Journal of Climate*, *27*(7), 2667–2681. <https://doi.org/10.1175/JCLI-D-13-00577.1>
- Wittenberg, A. T., Vecchi, G. A., Delworth, T. L., Rosati, A., Anderson, W., Cooke, W. F., et al. (2018). Improved simulations of tropical Pacific annual-mean climate in the GFDL FLOR and HiFLOR coupled GCMs. *Journal of Advances in Modeling Earth Systems*, *10*(12), 3176–3220. <https://doi.org/10.1029/2018MS001372>
- Xiang, B., Harris, L., Delworth, T. L., Wang, B., Chen, G., Chen, J.-H., et al. (2021). S2S prediction in GFDL SPEAR: MJO diversity and teleconnections. *Bulletin of the American Meteorological Society*, *103*(2), E463–E484. <https://doi.org/10.1175/BAMS-D-21-0124.1>
- Yan, X., Zhang, R., & Knutson, T. R. (2018). Underestimated AMOC variability and implications for AMV and predictability in CMIP models. *Geophysical Research Letters*, *45*(9), 4319–4328. <https://doi.org/10.1029/2018GL077378>
- Yan, X., Zhang, R., & Knutson, T. R. (2019). A multivariate AMV index and associated discrepancies between observed and CMIP5 externally forced AMV. *Geophysical Research Letters*, *46*(8), 4421–4431. <https://doi.org/10.1029/2019GL082787>
- Yano, J.-I., & Maarten, H. P. A. (2017). Moist static energy: Definition, reference constants, a conservation law and effects on buoyancy. *Quarterly Journal of the Royal Meteorological Society*, *143*(708), 2727–2734. <https://doi.org/10.1002/qj.3121>
- Zelinka, M. D., Myers, T. A., McCoy, D. T., Po-Chedley, S., Caldwell, P. M., Ceppi, P., et al. (2020). Causes of higher climate sensitivity in CMIP6 models. *Geophysical Research Letters*, *47*(1), e2019GL085782. <https://doi.org/10.1029/2019GL085782>
- Zhang, R., & Thomas, M. (2021). Horizontal circulation across density surfaces contributes substantially to the long-term mean northern Atlantic Meridional Overturning Circulation. *Communications Earth & Environment*, *2*(112). <https://doi.org/10.1038/s43247-021-00182-y>
- Zhao, J., & Johns, W. (2014). Wind-forced interannual variability of the Atlantic meridional overturning circulation at 26.5°N. *Journal of Geophysical Research: Oceans*, *119*(4), 2403–2419. <https://doi.org/10.1002/2013jc009407>
- Zhao, M., Golaz, J.-C., Held, I., Guo, H., Balaji, V., Benson, R., et al. (2018a). The GFDL global atmosphere and land model AM4. 0/LM4.0: 1. Simulation characteristics with prescribed SSTs. *Journal of Advances in Modeling Earth Systems*, *10*(3), 691–734. <https://doi.org/10.1002/2017ms001208>

- Zhao, M., Golaz, J.-C., Held, I. M., Guo, H., Balaji, V., Benson, R., et al. (2018b). The GFDL global atmosphere and land model AM4. 0/LM4.0: 2. Model description, sensitivity studies, and tuning strategies. *Journal of Advances in Modeling Earth Systems*, *10*(3), 735–769. <https://doi.org/10.1002/2017ms001209>
- Zhao, M., Golaz, J.-C., Held, I. M., Ramaswamy, V., Lin, S.-J., Ming, Y., et al. (2016). Uncertainty in model climate sensitivity traced to representations of cumulus precipitation microphysics. *Journal of Climate*, *29*(2), 543–560. <https://doi.org/10.1175/JCLI-D-15-0191.1>
- Zhou, L., Lin, S.-J., Chen, J.-H., Harris, L., Chen, X., & Rees, S. L. (2019). Toward convective-scale prediction within the next generation global prediction system. *Bulletin of the American Meteorological Society*, *100*(7), 1225–1243. <https://doi.org/10.1175/BAMS-D-17-0246.1>